

Kinematics in Young Star Clusters and Associations with Gaia DR2

MICHAEL A. KUHN,¹ LYNNE A. HILLENBRAND,¹ ALISON SILLS,² ERIC D. FEIGELSON,³ AND KONSTANTIN V. GETMAN³

¹*Department of Astronomy, California Institute of Technology, Pasadena, CA 91125, USA*

²*Department of Physics & Astronomy, McMaster University, 1280 Main Street West, Hamilton, ON L8S 4M1, Canada*

³*Department of Astronomy & Astrophysics, 525 Davey Laboratory, Pennsylvania State University, University Park, PA 16802, USA*

(Received July 5, 2018; Revised July 5, 2018)

Submitted to AAS Journals

ABSTRACT

The *Gaia* mission has opened a new window into the internal kinematics of young star clusters at the sub-km s⁻¹ level, with implications for our understanding of how star clusters form and evolve. We use a sample of 28 clusters and associations with ages from ~ 1 –5 Myr, where cluster members are already known from previous X-ray, optical, and infrared studies. Proper motions from *Gaia* DR2 reveal that 70% of these clusters show signs of expansion, with typical expansion velocities of ~ 0.5 km s⁻¹. Furthermore, in many expanding associations, there is a positive radial gradient in the expansion velocity. We consider NGC 6530 and the Orion Nebula Cluster (ONC) as prototypes for systems with and without expansion. Velocity dispersions among the sample clusters and associations range from $\sigma_{1D} = 1$ –3 km s⁻¹. NGC 6530 is gravitationally unbound, with $\sigma_{1D} = 2.2 \pm 0.2$ km s⁻¹ and expansion velocity 0.9 km s⁻¹, while the denser ONC is consistent with virial equilibrium, having $\sigma_{1D} = 1.8 \pm 0.1$ km s⁻¹ and a Gaussian velocity distribution. The ONC also has a nearly constant velocity dispersion as a function of radius, but another non-expanding cluster, NGC 6231, has a velocity dispersion that decreases with radius. For those star-forming regions that contain multiple clusters or subclusters, we examine the kinematics of the individual groups and find that there is no evidence for ongoing coalescence of these groups. We compare our results to a cluster formation simulation, and comment on the implications for cluster assembly and the role of gas expulsion in cluster dissipation.

Keywords: astrometry; stars: formation; stars: kinematics and dynamics; open clusters and associations: individual (Berkeley 59, Carina Nebula, Cep OB3b, IC 348, IC 5146, LkH α 101, M17, M20, Mon R2, NGC 1333, NGC 1893, NGC 2244, NGC 2264, NGC 2362, NGC 6231, NGC 6357, NGC 6530, NGC 6611, NGC 7160, Orion Nebula, RCW 120)

1. INTRODUCTION

While star formation in the Galaxy occurs in large star-forming complexes, most of the stars formed in these complexes quickly disperse into the field without remaining bound to one another as members of open clusters (Lada & Lada 2003; Gouliermis 2018). Star formation takes place in turbulent, clumpy giant molecular clouds, and yet the star clusters that do remain bound tend to have smooth stellar density distributions. The processes of cluster assembly, equilibration, and dissolution have remained poorly constrained by observation for two reasons: the difficulty of obtaining reliable samples of cluster members in nebulous regions with many

field star contaminants and the absence of kinematic information for faint stars. The nearby Orion Nebula Cluster (ONC) has been extensively characterized, but these difficulties have been overcome more recently for other massive star-forming complexes. In these regions, samples of members emerge from multi-wavelength surveys (Feigelson 2018), while the *Gaia* mission (Gaia Collaboration et al. 2016) is expected to revolutionize the study of their internal kinematics (Allison 2012; Clarke et al. 2015; Moraux 2016).

The kinematics of young stars should reflect the processes of star cluster formation. Two principal paths from theoretical studies are: “monolithic” cluster formation, in which a young star cluster is born in a single molecular cloud core, and “hierarchical” cluster formation, in which larger clusters are built via the accumulation of smaller subclusters (Elmegreen 2000; Bonnell et al. 2003; Banerjee & Kroupa 2015). Young stellar

objects (YSOs) that are embedded or partially embedded in star-forming clouds typically have clumpy distributions, where groups are known as subclusters (e.g., Aarseth & Hills 1972; Lada & Lada 1995; Kuhn et al. 2014; Megeath et al. 2016; Sills et al. 2018). It has been unclear, however, whether the subclusters will disperse once the molecular gas disperses, or if they will merge into larger, possibly bound clusters that survive gas expulsion. Examination of the motions of these subclusters can help constrain cluster formation scenarios.

The evolution of a young cluster depends on its dynamical state (e.g., Parker et al. 2014; Sills et al. 2018), as well as changes in the gravitational potential due to the dispersal of the molecular cloud (e.g., Tutukov 1978; Hills 1980) and tidal interactions with clouds and clusters (e.g., Kruijssen 2012). Much attention has been focused on the role of gas expulsion, which will cause a cluster to expand and possibly cause bound embedded clusters to become unbound (Mathieu 1983; Elmegreen 1983; Adams 2000; Kroupa et al. 2001; Goodwin & Bastian 2006; Pelupessy & Portegies Zwart 2012; Brinkmann et al. 2017). However, recent simulations have suggested that gas expulsion may play a less important role in cluster disruption if there is spatial decoupling between stars and gas (Dale et al. 2015).

The empirical relationship between size and density of young star clusters and associations provides indirect evidence for their expansion (Pfalzner 2009, 2011; Pfalzner et al. 2014). For subclusters, size has been found to be negatively correlated with density, and positively correlated with age, as would be expected if they were expanding (Kuhn et al. 2015a; Getman et al. 2018a). Furthermore, Marks & Kroupa (2012) argue that the low binary fractions observed in young star clusters imply these clusters were more compact upon formation.

Direct evidence of cluster expansion via proper-motion measurements has been difficult to obtain. There has long been debate about whether the ONC is expanding or contracting (Muench et al. 2008). In recent work, Dzib et al. (2017) find no evidence of expansion or contraction of the ONC using proper motions from radio observations, while Da Rio et al. (2017) report a correlation between radial velocity (RV) and extinction that can be explained by expansion, and Kounkel et al. (2018) report a preference for expansion among stars around the outer edges of Orion A. Recent studies of OB associations have yielded no evidence of expansion (Wright et al. 2016; Wright & Mamajek 2018; Ward & Kruijssen 2018).

In this paper, we use the superb astrometry of *Gaia*'s Second Data Release (DR2; Gaia Collaboration et al. 2018a) to elucidate the formation (evidence for or against hierarchical assembly) and dynamical state (expansion, contraction, or equilibrium) of young star clusters. We use a sample of young star clusters and associations, ranging from 0.3–3.7 kpc, that were the focus of a series of studies combining NASA's *Chandra*

X-ray, *Spitzer* mid-infrared, and ground-based optical and near-infrared images to provided reliable samples of tens-of-thousands of YSOs (Feigelson et al. 2013; Getman et al. 2017; Kuhn et al. 2017b).

2. DATA SETS

2.1. YSOs in Clusters and Associations

Our YSO sample is based on the X-ray/infrared catalogs from the Massive Young Star-Forming Complex Study in Infrared and X-ray survey (MYStIX; Broos et al. 2013; Feigelson et al. 2013), the Star-Formation in Nearby Clouds study (SFINC; Getman et al. 2017), and a similar catalog for NGC 6231 (Kuhn et al. 2017b). In each of these studies, X-ray emission was used to classify probable cluster members based on the higher expected X-ray luminosities of pre-main-sequence stars compared to main-sequence field stars. MYStIX and SFINC also include sources selected by infrared excess, which indicates YSOs with disks and envelopes that may or may not be X-ray emitters. The infrared-selected samples come from Povich et al. (2013) and Getman et al. (2017), with careful attention to reduce contamination by post-main-sequence dusty red giants. Reducing field star contamination is particularly important for these massive star forming regions that lie in the Galactic Plane.

In this study, we include only the regions that contain rich clusters visible in the optical. We omit the regions with few stars, and those for which *Gaia* is limited by high optical extinction (e.g., Serpens South or DR 21). These criteria yield a sample of 28 star clusters and associations which reside in 21 star-forming regions (Table 1).

In this paper, we use the term “cluster” to indicate a statistical cluster of spatially associated stars, which includes embedded clusters, bound open clusters, and compact associations of unbound stars (Kuhn et al. 2014). Some of the regions contain multiple clusters that are analyzed individually. Notable examples include NGC 2264 (containing a loose association around S Mon and embedded clusters around IRS 1 and IRS 2 adjacent to the Cone Nebula), NGC 6357 (containing Pismis 24, G353.1+0.36, and G353.2+0.7), the Carina Nebula (including Tr 14, Tr 15, and Tr 16), and the Cep OB3b association (containing a group to the east adjacent to the Cep B cloud and a group to the west around V454 Cep). For the Rosette Nebula region, which includes stars both in the cluster NGC 2244 and in the Rosette Molecular Clouds, we use only NGC 2244 for expansion analysis. In the Orion star-forming region, we focus only on the Orion Nebula Cluster (ONC). The sample of 28 clusters is given in Table 1.

2.2. Cross-matching to *Gaia* DR2

Our study is primarily based on astrometric measurements from the *Gaia* DR2 catalog (Gaia Collaboration et al. 2018a; Lindegren et al. 2018). We use the astrometric notation α and δ for right ascension and decli-

nation, ϖ for parallax in units of milliarcseconds (mas) and μ_{α^*} and μ_{δ} for proper motions in units of mas yr^{-1} , where $\mu_{\alpha^*} \equiv \mu_{\alpha} \cos \delta$.

We cross-matched 30,839 objects from the YSO catalogs to sources in the *Gaia* catalog. Significant effort has already been devoted to identifying the best match between X-ray and optical/infrared sources in the MYStIX, SFiNCs, and NGC 6231 catalogs (e.g., Naylor et al. 2013; Getman et al. 2017). The optical or infrared source coordinates are often more precise than the X-ray positions, and in such cases we use those coordinates for cross-matching with *Gaia*. The match radius for matching to *Gaia* sources was set to 1.2 arcsec, and we select the nearest *Gaia* source within that match radius.

The cross matching lead to 20,716 matches with the *Gaia* DR2 catalog, 17,509 of which have the 5-parameter “astrometric global iterative solution” (AGIS) involving position, parallax, and proper motion (Lindgren et al. 2018). The median magnitude of these sources is $G = 18.1$ mag (inter-quartile range: 16.6–19.1 mag) and the median proper-motion precision is $\sigma_{\mu} = 0.4 \text{ mas yr}^{-1}$ (inter-quartile range: 0.2–0.8 mas yr^{-1}). The *Gaia* catalog includes statistical uncertainties on astrometric properties calculated from the astrometric model. For AGIS models that do not converge, solutions are provided with relaxed criteria, with up to 20 mas of astrometric excess noise as defined by Lindgren et al. (2012). We only accept sources with `astrometric_excess_noise` < 1 mas as providing reliable kinematics. We also omit likely non-member contaminants (Section 3.3) and sources with statistical uncertainties $> 3 \text{ km s}^{-1}$ on tangential velocity (Section 3.4). The final sample contains 6475 objects.

In Figure 1 the left panel shows a near-infrared color-magnitude diagram for both the full catalog of YSOs in NGC 6530 and the subsample used for the *Gaia* analysis. In this region, at a distance of $d = 1.33$ kpc, the *Gaia* sources include stars down to $\sim 0.5 M_{\odot}$, and tend to be the least absorbed sources. The right panel shows proper motions, and their uncertainties, as a function of *Gaia*’s G magnitude for these sources. The mass range of the *Gaia* sample is different in different regions, depending on distance and extinction. However, in nearly all the regions, stars down to $0.5\text{--}1 M_{\odot}$ are included. Several nearby regions have *Gaia* data that probes to even lower mass stars, notably NGC 1333, IC 348, the ONC, and NGC 2264. Conversely, our sample for the

distant region NGC 1893 contains only stars with masses $> 2 M_{\odot}$.

The presence of a visual binary or the acceleration of a source can cause the *Gaia* astrometric solution to be rejected (Lindgren et al. 2018). Nevertheless, astrometric binaries remain a possible contributor to scatter in proper motion distributions. The velocity dispersion due to binaries depends on the individual stellar masses, binary separations, eccentricity of orbits, and inclinations of the systems. Binary orbital motions are unlikely to have a preferential orientation, so they should not bias observed bulk shifts in velocity, but they can contribute a high-velocity tail to velocity distributions.

The effect of binaries on velocity dispersions can be partially mitigated by filtering out sources with high astrometric excess noise. We use the ONC as a testbed to examine the link between binarity and astrometric excess noise. Duchêne et al. (2018) provides a list of ONC stars with and without companions at separations of 10–60 AU, based on HST imaging. For the visual binaries, 50% have `astrometric_excess_noise` > 1 mas, while only 7% of the non-visual binary stars in their sample exceed this threshold. This result supports our decision to only use sources below a 1 mas threshold for measuring median properties of stellar kinematics. We also note that the well-known O-star system, θ^1 Ori C, has `astrometric_excess_noise` > 1 mas, and thus is not included in our sample. For applications that require accurate estimates of measurement uncertainty, such as measuring velocity dispersions, we limit the sample to data with `astrometric_excess_noise` = 0 mas.

2.3. Subclusters

Subclusters in the star-forming regions studied here were cataloged by Kuhn et al. (2014) for MYStIX, Getman et al. (2018a) for SFiNCs, and Kuhn et al. (2017a) for NGC 6231. Subcluster identification in these papers was based on mixture models, a statistical cluster analysis method that is well adapted to cases where size and density of clusters can vary and the number of clusters is uncertain (McLachlan & Peel 2000; Kuhn & Feigelson 2017). In some star-forming regions subclusters can be found outside the main cluster, while, in others, subclusters are clumps of stars that make up the main cluster. The kinematics of these groups are addressed in Section 6.

Table 1. Cluster/Association Sample

Region	α_0	δ_0	n_{samp}	$\mu_{\alpha^*,0}$	$\mu_{\delta,0}$	ϖ_0	distance
	J2000	J2000	stars	mas yr ⁻¹	mas yr ⁻¹	mas	pc
(1)	(2)	(3)	(4)	(5)	(6)	(7)	(8)
Berkeley 59	0 2 14.91	+67 25 7.6	224	-1.61±0.10	-1.92±0.09	0.91±0.04	1100 ⁺⁵⁰ ₋₅₀
NGC 1333	3 29 7.96	+31 20 39.3	47	7.47±0.29	-9.70±0.17	3.37±0.07	296 ⁺⁶ ₋₆
IC 348	3 44 33.88	+32 09 31.8	178	4.63±0.15	-6.44±0.13	3.10±0.05	323 ⁺⁵ ₋₅
LkH α 101	4 30 10.17	+35 16 4.9	63	2.20±0.21	-5.14±0.40	1.78±0.05	561 ⁺¹⁶ ₋₁₅
NGC 1893	5 22 53.74	+33 26 54.5	84	-0.24±0.08	-1.39±0.08	0.26±0.04	3780 ⁺⁷¹⁰ ₋₅₂₀
ONC	5 35 15.68	-05 23 40.1	377	1.48±0.11	0.50±0.12	2.48±0.04	403 ⁺⁷ ₋₇
Mon R2	6 7 47.58	-06 22 42.6	97	-2.91±0.11	1.05±0.18	1.06±0.05	948 ⁺⁴³ ₋₃₉
Rosette	6 32 26.76	+04 47 37.1	468	-1.63±0.07	0.15±0.07	0.64±0.04	1560 ⁺¹¹⁰ ₋₉₀
— NGC 2244	6 31 55.77	+04 55 7.8	272	-1.69±0.08	0.20±0.08	0.65±0.04	1550 ⁺¹¹⁰ ₋₉₀
NGC 2264	6 40 57.93	+09 40 49.0	516	-1.76±0.08	-3.72±0.07	1.35±0.04	738 ⁺²³ ₋₂₁
— S Mon	6 40 49.83	+09 51 3.3	241	-1.62±0.08	-3.72±0.08	1.36±0.04	738 ⁺²³ ₋₂₂
— IRS 2	6 41 0.59	+09 35 51.6	148	-2.29±0.13	-3.61±0.08	1.34±0.04	747 ⁺²⁵ ₋₂₃
— IRS 1	6 41 7.25	+09 28 10.1	126	-2.05±0.16	-3.90±0.09	1.36±0.04	736 ⁺²⁴ ₋₂₂
NGC 2362	7 18 42.90	-24 57 44.0	244	-2.83±0.08	2.94±0.08	0.75±0.04	1331 ⁺⁷⁷ ₋₆₉
Carina	10 45 2.23	-59 41 59.8	1285	-6.55±0.07	2.17±0.07	0.38±0.04	2620 ⁺³¹⁰ ₋₂₅₀
— Tr 14	10 44 1.68	-59 32 48.1	401	-6.54±0.07	2.06±0.07	0.38±0.04	2600 ⁺³¹⁰ ₋₂₅₀
— Tr 15	10 44 42.08	-59 22 40.6	194	-6.25±0.08	2.06±0.08	0.38±0.04	2600 ⁺³¹⁰ ₋₂₅₀
— Tr 16	10 44 53.49	-59 43 10.1	267	-6.91±0.07	2.62±0.08	0.38±0.04	2610 ⁺³¹⁰ ₋₂₅₀
NGC 6231	16 54 15.90	-41 49 59.0	615	-0.55±0.07	-2.17±0.07	0.59±0.04	1710 ⁺¹³⁰ ₋₁₁₀
RCW 120	17 12 23.88	-38 29 15.7	31	-0.81±0.13	-2.37±0.18	0.60±0.05	1680 ⁺¹⁵⁰ ₋₁₃₀
NGC 6357	17 25 18.73	-34 17 24.8	178	-0.90±0.08	-2.29±0.10	0.56±0.04	1770 ⁺¹⁴⁰ ₋₁₂₀
— Pismis 24	17 24 44.06	-34 13 20.3	76	-0.81±0.08	-2.07±0.10	0.56±0.04	1790 ⁺¹⁵⁰ ₋₁₃₀
— G353.1+0.6	17 25 34.09	-34 24 49.5	55	-0.95±0.10	-2.34±0.12	0.57±0.05	1770 ⁺¹⁶⁰ ₋₁₄₀
— G353.2+0.7	17 25 59.77	-34 16 4.4	48	-1.09±0.09	-2.65±0.13	0.56±0.05	1780 ⁺¹⁶⁰ ₋₁₄₀
M20	18 2 23.10	-23 01 50.0	114	0.42±0.11	-1.69±0.09	0.79±0.05	1265 ⁺⁷⁷ ₋₆₉
NGC 6530	18 4 14.84	-24 21 45.9	662	1.32±0.08	-2.06±0.08	0.75±0.04	1333 ⁺⁷⁶ ₋₆₈
NGC 6611	18 18 42.20	-13 47 3.0	353	0.21±0.08	-1.55±0.08	0.57±0.04	1750 ⁺¹⁴⁰ ₋₁₂₀
M17	18 20 28.50	-16 10 58.0	82	-0.03±0.17	-1.40±0.12	0.60±0.04	1670 ⁺¹³⁰ ₋₁₂₀
IC 5146	21 53 31.47	+47 15 54.5	110	-2.88±0.11	-2.50±0.16	1.28±0.04	783 ⁺²⁷ ₋₂₅
NGC 7160	21 53 46.36	+62 35 7.6	71	-3.53±0.10	-1.43±0.13	1.04±0.04	961 ⁺⁴¹ ₋₃₈
Cep OB3b	22 55 31.19	+62 38 54.1	676	-0.75±0.09	-2.31±0.08	1.16±0.04	863 ⁺³¹ ₋₂₉
— Cep B	22 56 40.29	+62 42 6.2	481	-0.62±0.10	-2.28±0.09	1.15±0.04	868 ⁺³² ₋₃₀
— V454 Cep	22 53 47.06	+62 35 46.6	195	-1.21±0.11	-2.63±0.11	1.18±0.04	847 ⁺³¹ ₋₂₉

NOTE—Column 1: Region name. Clusters that are part of larger star-forming complexes are indented. Columns 2–3: Coordinates of the cluster center. Column 4: The sizes of the sample of stars used in the analysis. Column 5–6: Proper motion of the cluster center. Column 7: Parallax of the cluster center.

3. BASIC CLUSTER PROPERTIES

3.1. *Parallaxes*

Cluster distance can be estimated with the assumption that cluster members span a small range of distances (cf. Bailer-Jones et al. 2018, their Section 3.2). This assumption is approximately true for our sample — the nearest region NGC 1333 has a diameter only $\sim 0.4\%$ of the distance to the cluster. *Gaia* parallax measurements can then be considered to be random variables drawn from a distribution where the mean is ϖ_0 , the parallax of the cluster center, and the standard deviation is the measurement uncertainties given in the *Gaia* catalog. Using multiple stars to estimate the parallax of the center of a cluster, ϖ_0 , will yield a measurement with smaller uncertainties than for the individual stars. However, gains in precision from pooling stars are limited due to correlated uncertainties of up to ~ 0.04 mas that are noticeable on spatial scales smaller than 1 degree (Lindgren et al. 2016).

We estimate cluster parallax using the weighted median of individual stellar parallax measurements. This method is robust against contaminants while taking into account the measurement uncertainties. For this analysis, we use the conventional $1/\text{error}^2$ weights and the *weighted.median* function from the CRAN package *spatstat* (Baddeley et al. 2015) within the *R* statistical software environment (R Core Team 2018). Uncertainties on the weighted median parallax are calculated using bootstrap analysis, with random sampling with replacement from the set of measurements (with added random errors) and weights. Finally, we add in quadrature the systematic uncertainty of 0.04 mas described by Lindgren et al. (2016), which provides a noise floor.¹

Table 1 provides the new parallax estimates that we use in this study. Parallaxes are calculated independently for each cluster in a star-forming complex; the nearly identical parallax measurements for different clusters in the same region provides confidence in the accuracy of the measurements and reassurance that these clusters are physically associated. In all cases, the uncertainties on median parallaxes are dominated by the systematic uncertainties in *Gaia* astrometry and not by statistical dispersion.

Several highlights from revised distances in Table 1 are mentioned here. Our analysis of the *Gaia* data places the ONC at a distance of 403_{-6}^{+7} pc, which is slightly closer than the estimate of 414 ± 7 pc from Menten et al. (2007), but farther than 388 ± 5 pc found by Kounkel et al. (2016b), both based on Very Long Baseline Ar-

ray (VLBA) data. In Appendix A we compare our distance estimate to 386 ± 8 pc from Kounkel et al. (2018) and discuss effects of the three-dimensional structure of Orion A. Our distance estimate for NGC 1333 of 296 ± 6 pc is $\sim 25\%$ larger than the distance from Hirota et al. (2008) of 235 ± 18 pc. A larger distance to NGC 1333 will move stellar age estimates downwards, which would resolve some anomalies in age estimates noted by Luhman et al. (2016) and Richert et al. (2018). Another interesting case is M20, where the *Gaia* distance estimate of 1270 ± 70 pc is a factor of ~ 2 nearer than the distance estimate of 2700 pc from Cambr es et al. (2011). The revised distance places M20 at a similar distance as NGC 6530, from which it is separated by only 1.4° on the sky.

3.2. *Proper Motions*

The proper motions of the cluster centers, $\mu_{\alpha^*,0}$ and $\mu_{\delta,0}$, are estimated using the same weighted-median strategy as above. For systematic uncertainties due to correlated errors, we use ± 0.07 mas yr⁻¹ (Lindgren et al. 2016). These proper motions are reported in Table 1. Given that the clusters each subtend < 1 degree on the sky, we ignore spherical geometry effects in determination of the median — the small corrections calculated below for individual stars do not affect the proper motion of the cluster center.

The effects of correlated errors in *Gaia* DR2 on relative velocities of stars within clusters was investigated in simulations by Bianchini et al. (2018). They found the effects were $< 0.5 \mu\text{as yr}^{-1}$ on length scales of 10 arcmin, which suggests that these effects will be negligible in our study of cluster kinematics.

3.3. *Refined Sample*

Parallax and proper motion measurements allow us to identify likely field-star contaminants in the MYSTIX/SFINCS/NGC6231 catalogs. Stars are removed from the sample if their parallax measurements are inconsistent with the median parallax by more than 3 standard deviations, taking into account uncertainty on the measurement and on the median. Proper motion is also used to filter out stars with values that are discrepant by > 5 standard deviations from the observed distribution.

Estimation of cluster parallax and proper motion and refinement of membership is performed iteratively until convergence. For example, in NGC 6231 with 1760 *Gaia* counterparts, 121 (7% of the total) are removed as likely contaminants, leaving 1639 *bona fide* cluster members in *Gaia*. (Only 615 of these have sufficient astrometric precision for inclusion in the analysis.) Overall, contamination rates were about 13%, with contamination rates for individual clusters mostly falling into the range 7–15%. Several clusters with much higher contamination among the *Gaia* sources include M17 (23%), NGC 2362

¹ Several papers have proposed correction factors for systematic errors in *Gaia* astrometry (e.g., Stassun & Torres 2018; Muraveva et al. 2018; Kounkel et al. 2018), all of which are consistent with the systematic uncertainties reported by Lindgren et al. (2016). The parallax and proper motion values reported in Table 1 are based on *Gaia* astronomy with no correction applied.

(25%), NGC 7160 (28%), and RCW 120 (38%). Table 1 gives the number of stars in the final, refined sample.

3.4. Stellar Kinematics

We are interested in obtaining two components of stellar velocities (from a three-dimensional Cartesian coordinate system) based on the proper motions μ_{α^*} and μ_{δ} . Since the clusters in our sample are sufficiently distant, compact, and slow-moving, the relative proper motions of their stars are dominated by their physical velocities, so only small correction factors, calculated below, are necessary.

Observed proper motions of stars in clusters can be affected by perspective and the motion of the center of the cluster (van Leeuwen 2009). In particular, radial motion of a cluster can produce an effect known as “perspective expansion” which is seen in *Gaia* measurements of globular clusters (Gaia Collaboration et al. 2018b), many of which have RVs of hundreds of kilometers per second. A first-order approximation to the perspective expansion can be obtained from Equation 13 in van Leeuwen (2009). Here, α_0 , δ_0 , ϖ_0 , $\mu_{\alpha^*,0}$ and μ_{δ_0} are the astrometric parameters of the cluster center, and $\Delta\alpha_i$ and $\Delta\delta_i$ are the difference in right ascension and declination between a cluster member and the cluster center. The equations for the additional shift in proper motion of a star are

$$\Delta\mu_{\alpha^*,\text{per}} \approx \Delta\alpha_i \left(\mu_{\delta,0} \sin \delta_0 - \frac{v_r \varpi_0}{\kappa} \cos \delta_0 \right) \quad (1)$$

$$\Delta\mu_{\delta,\text{per}} \approx -\Delta\alpha_i \mu_{\alpha^*,0} \sin \delta_0 - \Delta\delta_i \frac{v_r \varpi_0}{\kappa}, \quad (2)$$

where $\kappa = 4.74$ is the conversion factor from mas yr^{-1} to km s^{-1} at a distance of 1 kpc. The first term in each equation relates to motion in a spherical coordinate system while the second term relates to the apparent expansion/contraction of an object as it gets farther/nearer.

These equations, calculated using RVs in Appendix B, contribute small shifts to apparent stellar proper motions. Following the strategy recommended by Brown et al. (1997), these contributions can be subtracted from the observed proper motions (relative to the cluster center) to isolate the effects of internal kinematics. The region with the largest corrections is the Orion A cloud with corrections on the order of $\sim 0.07 \text{ mas yr}^{-1}$. Most other regions have corrections with magnitudes $< 0.02 \text{ mas yr}^{-1}$. Similarly, for regions spanning < 1 degree, projection effects of spherical geometry are small ($< 0.02\%$), and are not expected to affect science results.

The correction factors computed above allow us to approximate a two-dimensional velocity of each star $\mathbf{v} = (v_{\alpha}, v_{\delta})$, relative to the cluster center rest frame, where

$$v_{\alpha} \approx -\kappa \left(\frac{\Delta\mu_{\alpha^*,\text{obs}} - \Delta\mu_{\alpha^*,\text{per}}}{\varpi_0} \right) \quad (3)$$

$$v_{\delta} \approx \kappa \left(\frac{\Delta\mu_{\delta,\text{obs}} - \Delta\mu_{\delta,\text{per}}}{\varpi_0} \right). \quad (4)$$

The velocity components v_{α} and v_{δ} are parallel to lines of right ascension and declination, respectively. This coordinate system is approximately Cartesian for fields that do not span a wide range of right ascensions and declinations. Uncertainties on \mathbf{v} can be described by a covariance matrix $\Sigma_{\text{err},i}$. This is obtained from the covariance matrix for the astrometric solution, reconstructed from the DR2 catalog using Equation B.3 in Lindegren et al. (2018), and scaled by $(\kappa/\varpi)^2$ to convert angular motions into velocities. This covariance matrix does not include the systematic effects of uncertainties in cluster parallax or RV.

Velocities can also be expressed in different coordinate systems. For example, the outward and azimuthal components of the projected velocity with respect to the center of the cluster are

$$v_{\text{out}} = \mathbf{v} \cdot \hat{\mathbf{r}} \quad (5)$$

$$v_{\text{az}} = \mathbf{v} \cdot \hat{\boldsymbol{\phi}}, \quad (6)$$

where $\hat{\mathbf{r}}$ is a unit vector pointing away from the cluster center and $\hat{\boldsymbol{\phi}}$ is a unit vector pointing in the azimuthal direction relative to the cluster center. Uncertainty on a velocity component in the $\hat{\mathbf{u}}$ direction can be obtained from the covariance matrix

$$\sigma_{\text{err},i} = (\hat{\mathbf{u}}^T \Sigma_{\text{err},i} \hat{\mathbf{u}})^{1/2}. \quad (7)$$

3.5. Visualizations of Kinematics

Several approaches to visualization of the observed 4-dimensional kinematic structure of star clusters are shown in Figures 2, 3, and 4. The ONC and NGC 6530 are shown as examples, but plots for the other 26 clusters are available online as figure sets. In each case, we depict velocities in the rest frames of their cluster centers.

Kinematics of stars in clusters can be displayed using arrows to show velocity vectors for each star (Figure 2). In regions with large numbers of stars, these produce crowded plots that are difficult to interpret. The figure highlights sources with the highest-quality proper-motion measurements.

Figure 3 shows the direction of motion (no amplitude) for individual stars. The color of the arrowhead is also determined by the direction of motion (as indicated by the compass wheel) for clearer visualization. In an area of the diagram where arrowheads are mostly one color, the stars are mostly moving in one direction. The color saturation of the symbol is related to the statistical weighting of the data point. Only points with uncertainties $< 3 \text{ km s}^{-1}$ are shown, with the darkest points representing points with uncertainties $< 0.5 \text{ km s}^{-1}$. The X’s mark the cluster centers used for measuring outward velocities v_{out} .

Figure 4 shows the relationship between star positions and velocities. For each cluster, the four scatter plots show velocities perpendicular and parallel to each coordinate axis. A simple radial contraction or expansion

will produce a gradient in the $v_\alpha - R.A.$ and $v_\delta - Dec$ diagrams (upper left and lower right) but will not affect the other diagrams (upper right and lower left). The different patterns of stellar motion within different clusters are analyzed in the next section.

4. BULK CLUSTER MOTIONS

4.1. Contraction vs Expansion Velocities

Cluster expansion or contraction is observable as a bulk outward or inward motion of its stars. The expansion inferred from the age–size relationships found for clusters and subclusters in the MYStIX/SFiNCs samples are on the order of $\sim 0.25\text{--}1 \text{ km s}^{-1}$ (Kuhn et al. 2015a; Getman et al. 2018b), which would be detectable with *Gaia* in the star-forming regions in our sample.

Velocities that are preferentially oriented outward can be seen in some clusters, and not in others. Cluster expansion would show up as arrows pointing radially outward in Figure 2, coherent patterns in arrow direction and hue in Figure 3, and correlations in positions and velocity in Figure 4.

NGC 6530 exhibits these characteristics. Stellar velocity vectors are primarily oriented away from the center of the cluster, which appears as an gradient in the color of points on Figure 3 and is also seen in the orientation of arrows on Figures 2. There are also correlations between v_α and α and v_δ and δ (Figure 4) that are consistent with the expectations for an expanding cluster. In contrast, for the ONC, these figures show that stars with differently oriented velocity vectors are more mixed up and there is no significant correlation between position and velocity of stars.

We quantify cluster expansion (or cluster contraction) using the weighted median value of v_{out} for each cluster using all members of the “refined sample” of stars. Uncertainties on the median are calculated by bootstrap resampling, as earlier. The expansion velocities are provided in Table 2.

The distribution of v_{out} values that go into calculating the median are illustrated in Figure 5, with weighted kernel-density estimates (KDE) of v_{out} obtained with function *density* in *R*. Shifts of the distribution toward positive values indicate expansion while shifts to negative values indicate contraction.

From our sample, median v_{out} values are more likely to be directed outward than inward. Figure 6 shows a histogram of these expansion/contraction velocities and a histogram of the signal-to-noise, calculated as the ratio of the median v_{out} to the estimated uncertainty on the median v_{out} . Although most clusters show effect sizes $< 3\sigma$, the distribution is clearly shifted to the right from what would be expected if clusters had zero expansion and all non-zero measurements were due to measurement uncertainty. There are 6 clusters with statistically significant outward velocities at the $> 3\sigma$ level, while no individual clusters show statistically significant inward velocities at this level. The velocity shifts range from

-2.5 to $+2.5 \text{ km s}^{-1}$, but are predominantly positive with a mean value of 0.5 km s^{-1} .

Clusters with indications of expansion include NGC 1893 ($> 3\sigma$), NGC 2244 ($> 3\sigma$), Tr 14, Tr 15, Tr 16 ($> 3\sigma$), Pismis 24, G353.1+0.6, NGC 6530 ($> 3\sigma$), NGC 6611 ($> 3\sigma$), IC 5146, Cep B ($> 3\sigma$), and V454 Cep. Several clusters show little to no expansion or contraction. These include Berkeley 59, NGC 1333, IC 348, ONC, S Mon, NGC 2264 IRS 2, NGC 2362, NGC 7160. The clusters LkH α 101, Mon R2, NGC 2264 IRS 1, RCW 120, G353.2+0.7, and M20 are cases where the uncertainties are large enough that results are ambiguous.

Two clusters show signs of contraction, albeit not at a high significance level. M17 has a fairly fast contraction rate (-2.5 km s^{-1}), but the *Gaia* data is limited by high extinction in this region, so the result is only significant at the 2σ level. NGC 6231 has a fairly slow contraction velocity of -0.3 km s^{-1} . Contraction of this cluster would be interesting because NGC 6231 is physically larger than most clusters, giving it the appearance of having expanded in the past.

4.2. Radial Dependence of Expansion Velocity

Models for the expansion of OB associations suggest linear relationships between expansion velocity and distance of stars from a cluster center (Blaauw 1964; Brown et al. 1997). This occurs because, in an unbound system, faster stars will travel farther from their point of origin, causing the stars to spatially sort themselves by velocity.

Figure 7 shows expansion velocity as a function of radius. For this plot, stars are binned by radial distance using bin sizes of ~ 60 stars, and expansion velocities are estimated using the same method as above. We fit the points with a line of the form $y = ax + b$ using weighted least squares regression, where weights are proportional to the reciprocal of the uncertainty squared. The slopes of regression lines have units of $\text{km s}^{-1} \text{ pc}^{-1}$ ($\approx \text{Myr}^{-1}$) and intercepts have units of km s^{-1} .

For the ONC, which shows little evidence for expansion, all points are consistent with the mean value. Both slope (0.1 ± 0.4) and intercept (0.3 ± 0.3) are consistent with there being no expansion. For NGC 6530, most of the points follow a positive linear relationship between radius and expansion velocity, and the two points that deviate from this relationship have large uncertainties. The slope of 0.8 ± 0.2 is statistically significant, while the intercept 0.5 ± 0.3 is not statistically significant. The regression analysis, using the *lm* function in *R*, gives a *p*-value of 0.002, providing definitive evidence that NGC 6530 has a radially dependent expansion velocity.

Several other clusters fall into each class. Examples that illustrate possible linear relationships between ra-

Table 2. Bulk Expansion and Rotation Velocities

Region	n_{samp} stars	median v_{out} km s ⁻¹	median v_{az} km s ⁻¹
(1)	(2)	(3)	(4)
Berkeley 59	224	0.26±0.21	-0.38±0.30
NGC 1333	47	0.22±0.29	-0.45±0.22
IC 348	178	0.06±0.15	-0.3±0.22
LkHα 101	63	0.98±0.68	0.78±0.42
NGC 1893	84	1.26±0.43	0.16±0.52
ONC	377	0.36±0.20	-0.35±0.15
Mon R2	97	-0.12±0.50	0.58±0.32
NGC 2244	272	1.20±0.23	-0.1±0.22
S Mon	241	0.39±0.14	-0.04±0.09
NGC 2264 IRS 2	148	-0.29±0.26	0.03±0.18
NGC 2264 IRS 1	126	0.32±0.39	-0.21±0.32
NGC 2362	244	0.12±0.26	-0.19±0.16
Tr 14	401	0.53±0.27	0.51±0.19
Tr 15	194	0.63±0.39	1.73±0.46
Tr 16	267	0.87±0.25	-0.01±0.34
NGC 6231	615	-0.31±0.14	-0.07±0.18
RCW 120	31	-0.20±1.40	-0.13±0.56
Pismis 24	76	0.83±0.41	0.40±0.51
G353.1+0.36	55	2.21±0.99	0.25±0.56
G353.2+0.7	48	-0.14±0.71	-1.09±0.48
M20	114	0.32±0.37	-0.20±0.39
NGC 6530	662	0.90±0.22	-0.32±0.17
NGC 6611	353	0.90±0.25	0.37±0.20
M17	82	-2.49±1.24	0.06±1.18
IC 5146	110	0.49±0.26	0.14±0.46
NGC 7160	71	-0.20±0.28	0.2±0.22
Cep B	481	0.94±0.31	0.6±0.15
V454 Cep	195	0.73±0.46	-0.20±0.36

NOTE—Column 1: cluster name. Column 2: Number of stars used to calculate median velocities. Column 3: Median v_{out} – measure of expansion or contraction. Column 4: Median v_{az} – measure of rotation.

dus and expansion rate include Cep B ($p = 0.02$), NGC 2244 ($p = 0.006$), and Tr 16 ($p = 0.08$). For these clusters, the slopes of the relationships range from ~ 0.5 to $1 \text{ km s}^{-1} \text{ pc}^{-1}$. Others clusters like Be 59, NGC 2362, NGC 6231, S Mon, Tr 14, and Tr 15 show flat relationships – the latter group includes both clusters with and without evidence for net expansion.

4.3. Cluster Rotation

The stellar velocity measurements can also be used to look for evidence of bulk rotation. The angular momentum of a star with mass m and velocity \mathbf{v} at a position \mathbf{r} relative to the center of the cluster is

$$\mathbf{L} = \mathbf{r} \times m \mathbf{v}, \quad (8)$$

so the component of the angular momentum along the line of sight is

$$L \cos i = -m R v_{\text{az}}, \quad (9)$$

where i is the inclination of the angular momentum vector and R is the projected distance of the star from the center of the cluster. Thus, a non-zero median value of v_{az} can indicate bulk rotation of a cluster. For v_{az} , we use the same method to calculate the median and error on the median that we used for v_{out} . These values are provided in Table 2.

For the 28 clusters in the sample, the values of median v_{az} are distributed around zero with an average of $0.06 \pm 0.10 \text{ km s}^{-1}$. For most clusters, the value of median v_{az} is within 2σ of $v_{\text{az}} = 0 \text{ km s}^{-1}$. A few cases have more statistically significant values, including LkHα 101, the ONC, Tr 14, and G353.2+0.7 at 2σ significance, and Tr 15 (median $v_{\text{az}} = 1.7 \text{ km s}^{-1}$) at 4σ significance. Typical uncertainties on median azimuthal velocities are $< 0.4 \text{ km s}^{-1}$, so cluster rotational velocities less than this value may not be detectable.

Under the assumption that the median values of v_{az} are all results of measurement uncertainty, the ratios of these values to their uncertainties should be drawn from a normal distribution with a mean 0 and standard deviation 1. Figure 8 shows a histogram of the ratio of observed rotation to measurement uncertainty, which is compared to the normal distribution expected given the null hypothesis. The distributions are remarkably similar, suggesting that no real rotation is detected in most of the clusters. However, Tr 15 is difficult to explain using the null hypothesis, so rotation may be real in this individual case.

Although bulk rotation has been reliably measured in globular clusters (e.g. Kamann et al. 2018; Bianchini et al. 2018), very few attempted measurements exist in the literature for open clusters. A recent study of *Gaia* DR1 data by Reino et al. (2018) concluded that there was no evidence for bulk rotation in the ~ 600 Myr old Hyades cluster, based on measurement of azimuthal motion at only the 2σ level. Our results are consistent with cluster rotation being rare, but we are less sensitive to rotational velocities below several tenths of a km s^{-1} .

Table 3. Velocity Dispersions in Select Clusters

Region	n_{samp}	σ_{1D}	σ_{pc1}	σ_{pc2}	$\sigma_{pc1}/\sigma_{pc2}$	PA	η_{outliers}	σ_{outliers}	ΔBIC
	stars	km s ⁻¹	km s ⁻¹	km s ⁻¹		degrees	%	km s ⁻¹	
(1)	(2)	(3)	(4)	(5)	(6)	(7)	(8)	(9)	(10)
Berkeley 59	19	1.2±0.2	1.5±0.3	0.8±0.2	2.0±0.6	177			
NGC 1893	56	2.4±0.3	3.1±0.4	1.3±0.5	2.3±0.9	38	19±11	6.5	-18
ONC	50	1.8±0.1	2.1±0.2	1.4±0.1	1.5±0.2	174			
Mon R2	13	1.7±0.4	2.0±0.5	1.4±0.6	1.4±0.7	3			
NGC 2244	93	2.1±0.1	2.3±0.2	1.8±0.2	1.2±0.2	26			
S Mon	68	1.1±0.1	1.3±0.1	0.9±0.1	1.4±0.2	88			
NGC 2264 IRS 2	29	1.5±0.2	1.6±0.2	1.3±0.2	1.2±0.3	68			
NGC 2264 IRS 1	31	1.6±0.2	2.0±0.3	1.0±0.2	2.0±0.4	74			
NGC 2362	99	0.8±0.1	0.9±0.1	0.7±0.1	1.2±0.3	152	15±12	2.2	-7.3
Tr 14	157	2.6±0.2	3.0±0.2	2.1±0.3	1.4±0.3	49	19.4±7.5	7.1	-51
Tr 15	108	2.4±0.2	2.5±0.2	2.3±0.2	1.1±0.1	105	10.9±4.6	9.4	-35
Tr 16	130	2.8±0.2	3.5±0.4	1.9±0.2	1.9±0.3	125	8.3±8.7	5.4	5.2
NGC 6231	298	1.6±0.1	1.8±0.1	1.5±0.1	1.2±0.1	144	10.7±3.8	5.6	-124
M20	36	1.6±0.2	1.9±0.3	1.2±0.2	1.6±0.4	74	11±10	6.1	-19
NGC 6530	190	2.2±0.1	2.6±0.2	1.7±0.2	1.5±0.2	107	15.9±7.6	5.4	-37
NGC 6611	99	1.8±0.2	2.2±0.3	1.3±0.2	1.6±0.4	20	22±8.4	5.8	-41
IC 5146	12	0.9±0.2	1.1±0.2	0.7±0.2	1.5±0.5	173			
NGC 7160	25	1.5±0.2	1.8±0.2	1.1±0.2	1.7±0.4	51			
Cep B	27	1.9±0.2	2.1±0.3	1.6±0.3	1.3±0.3	176			

NOTE—Column 1: Cluster name. Column 2: Number of stars used to calculate velocity dispersions. Column 3: Characteristic one-dimensional velocity dispersion. Column 4–5: Velocity dispersion in the first and second principal components for the two-dimensional velocity model. Column 6: Ratio of velocity dispersions in the first and second velocity principal components – a measure of overall velocity anisotropy. Column 7: Position angle (east from north) of the semi-major axis of the velocity dispersion. Column 8: Fraction of stars belonging to the second component of the mixture model. Column 9: Velocity dispersion for the second component of the mixture model. Column 10: Change in BIC when the second component was added. The last three columns are only used when a multiple component velocity model was required.

5. VELOCITY DISPERSIONS

Calculation of velocity dispersion is particularly sensitive to measurement errors, which can broaden the observed distribution. The astrometric measurement uncertainties reported in the *Gaia* catalog are heteroscedastic and comparable to the velocity dispersion, so their effect must be carefully modeled. For *Gaia* sources with `astrometric.excess_noise` > 0, the statistical uncertainties derived from the *Gaia* DR2 AGIS model may not represent the real errors in relative proper motions (Lindegren et al. 2012). Thus, we use only sources with `astrometric.excess_noise` = 0 when modeling velocity distributions.

We use maximum likelihood to estimate the intrinsic velocity dispersion in the presence of measurement error (cf. Walker et al. 2006). We model the observed velocity of a star i as the sum of its intrinsic velocity \mathbf{v}_i and an error term $\boldsymbol{\epsilon}_i$,

$$\mathbf{v}_{\text{obs},i} = \mathbf{v}_i + \boldsymbol{\epsilon}_i. \quad (10)$$

Both \mathbf{v}_i and $\boldsymbol{\epsilon}_i$ are assumed to be multivariate normally distributed, with

$$\mathbf{v}_i \sim N(\boldsymbol{\mu}_v, \Sigma_v) \quad (11)$$

$$\boldsymbol{\epsilon}_i \sim N(\mathbf{0}, \Sigma_{\text{err},i}), \quad (12)$$

where $\boldsymbol{\mu}_v$ and Σ_v are the mean and covariance matrix of the intrinsic velocity distribution, and $\Sigma_{\text{err},i}$ is the covariance matrix for measurement uncertainty on the i th star. Then the log-likelihood is

$$\mathcal{L}(\boldsymbol{\mu}_v, \Sigma_v | \mathbf{v}_{\text{obs},i}, \Sigma_{\text{err},i}) = \sum_{i=1}^N \log \phi(\boldsymbol{\mu}_v, \Sigma_v + \Sigma_{\text{err},i}), \quad (13)$$

where ϕ is the probability density of the normal distribution. The maximum likelihood $\boldsymbol{\mu}_v$ and Σ_v parameters can be found by numerical optimization. We used the BFGS algorithm (Fletcher & Reeves 1964) implemented in the *R* function `optim`. Examination of the likelihood function shows it to be approximately normal, so we use `optim` to numerically calculate the Hessian matrix at the maximum (also called the Fisher Information Matrix) and invert it to estimate the covariance matrix.

5.1. Velocity Phase Space

The total velocity dispersions of the individual clusters will incorporate both the bulk expansion velocity (if non-zero) and a velocity spread due to the orbital motions of individual stars. Figure 9 shows stars plotted in velocity phase space with coordinates (v_α, v_δ) , where the ONC and NGC 6530 are used as examples.

The observed velocity distributions are not entirely isotropic. Stars in the ONC are preferentially moving north or south, rather than east or west, while stars in NGC 6530 are preferentially moving east or west, rather than north or south. However, the referencing of stellar motions to a frame that is based on the equatorial coordinate system is arbitrary.

The Gaussian model of the velocity distribution provides two velocity dispersion components. These are the two principal components of the velocity dispersion, where the first component is defined to be the one with the largest variance. Thus σ_{pc1} is the semi-major axis of the ellipses in Figure 9, while σ_{pc2} , is the semi-minor axes. The use of Equation 13 allows for the heteroscedastic uncertainties to be taken into account in the principal component analysis. Table 3 provides σ_{pc1} , σ_{pc2} , as well as their ratio and the position angle of the first principal component, as well as their errors.

The ratios of σ_{pc1} to σ_{pc2} show that most clusters do not have statistically significant velocity anisotropy (i.e. values that are significantly greater than 1). However, the ONC has $\sigma_{pc1}/\sigma_{pc2} = 1.5$ at 2.5σ significance and NGC 6530 has $\sigma_{pc1}/\sigma_{pc2} = 1.4$ at 3σ significance. In both cases, the orientation of the velocity anisotropy is approximately aligned with the spatial elongation of the cluster.

5.2. Shape of the Velocity Distribution

We can examine the shape of velocity distributions by comparison to bivariate normal distributions. Henze & Zirkler (1990) provide a test of multivariate normality, implemented in the *R* package *MVN* (Korkmaz et al. 2014). The clusters where velocity distributions are consistent with multivariate normal distributions include Berkeley 59, the ONC, IRS 1, and IC 5146 ($p > 0.05$). The clusters Mon R2, NGC 2244, NGC 7160, and Cep B show moderate statistically significant deviation from normality ($0.05 < p < 0.001$), while NGC 1893, S Mon, IRS 2, NGC 2362, Tr 14/15/16, NGC 6231, M20, NGC 6530, and NGC 6611 show large statistically significant deviations from normality ($p < 0.001$). We note that this hypothesis test is more sensitive to deviations when sample sizes are larger and it does not indicate how the distribution deviates from normality.

Deviations from normality can be visualized using plot of observed data quantiles versus theoretical quantiles (Q-Q plot). The data quantiles are the difference between the each measurement and the mean value, normalized by the standard deviation,

$$Q_{\text{data},i} = \frac{v_{\text{obs},i} - \mu}{\sqrt{\sigma_v^2 + \sigma_{\text{err},i}^2}} \quad (14)$$

while the theoretical quantiles are

$$Q_{\text{theo},i} = \sqrt{2} \text{erf}^{-1}(2(r_i - 0.5)/n - 1), \quad (15)$$

the quantile function of the Gaussian distribution, where n is the number of velocity measurements, r_i is the rank of the i th measurement, and erf^{-1} is the inverse of the error function. We calculate a test envelope (95%) for the null hypothesis that the data are correctly described by our model using Monte Carlo simulations.

Q–Q plots are produced for each velocity component (Figure 10). The ONC velocity distribution is remarkably well fit by a normal distribution. This result is astrophysically interesting in itself (see Section 8), but also implies that standard deviations of the distribution calculated using Equation 13 will be reliable.

For NGC 6530, the distribution closely follows a normal distribution out to $\pm 2\sigma$, but beyond this threshold there is a significant excess of stars with higher velocities than would be expected from a normal distribution. Even a small number of outliers can have a large effect on estimates of standard deviation, so the observed deviations from a normal distribution suggest that a standard deviation estimated from Equation 13 will overestimate the width of the distribution.

For nearly half the clusters, the shape of the observed velocity distribution indicates the presence of outliers. The nature of the outliers is uncertain. While these could represent a population of higher velocity stars that are escaping the cluster at a faster rate, they could also represent points with large errors not represented well by the AGIS uncertainties or field stars contaminating the “refined sample.” In Table 3, the more distant clusters tend to be the ones where outliers are detected. While the astrometric excess noise parameter is effective at flagging known binary stars in the ONC, it is not likely to be as effective for more distant regions. Overall, the outliers do not seem to have a preferential spatial location within the clusters.

A possible strategy to cope with outliers is to use a mixture model to represent the main population and the outliers as two distinct Gaussian components. In our model, these components will have the same means but different covariance matrices (cf. Bravi et al. 2018). The complete data likelihood for this mixture model is

$$\mathcal{L}(\boldsymbol{\mu}_v, \Sigma_{v,1}, \Sigma_{v,2}, \eta | \mathbf{v}_{\text{obs},i}, \Sigma_{\text{err},i}) = \sum_{i=1}^N \log((1 - \eta) \phi(\boldsymbol{\mu}_v, \Sigma_{v,1} + \Sigma_{\text{err},i}) + \eta \phi(\boldsymbol{\mu}_v, \Sigma_{v,2} + \Sigma_{\text{err},i})), \quad (16)$$

where $\Sigma_{v,1}$ and $\Sigma_{v,2}$ are the covariance matrices describing the velocity distribution and $0 < \eta < 1$ is the mixing parameter. For the second component, we use a radially symmetric normal distribution (i.e. $\Sigma_{v,2} = a I_n$) and require the dispersion to be larger than for the first component. If the second component is significantly wider than the first but has a much smaller fraction of the stars, than it can be considered a model for the “outliers.”

For star clusters where outliers can be seen on the Q–Q plot, we use Equation 16 to estimate the velocity dispersion of the main component, the fraction of sources that are outliers (the mixing parameter η in the model), and a velocity dispersion for the outliers. For both the single component and the mixture model, we calculate

the change in the Bayesian Information Criterion (BIC), which is a penalized likelihood used for selecting between models with different numbers of parameters where the model with the lowest BIC is preferred (Schwarz et al. 1978). For cases where the model appears to correctly identify outliers (i.e. η is small and the velocity dispersion is large for the second component) we report values from the mixture model method in Table 3. In 8 out of 9 cases where this model was applied, the two-component model produced a significant improvement in the BIC ($\Delta BIC < -6$). We note that in all cases where the outlier model improves the fit, Henze-Zirklers test showed strong deviation from normality.

5.3. One-Dimensional Velocity Dispersions

Formulas for cluster dynamics are often given in terms of a one-dimensional velocity dispersion, σ_{1D} , because this quantity can be obtained from radial velocity measurements alone. A characteristic one-dimensional velocity dispersion can also be obtained from multi-dimensional velocity dispersions by taking the mean variance

$$\sigma_{1D}^2 = \frac{\sigma_{\text{pc}1}^2 + \sigma_{\text{pc}2}^2}{2}. \quad (17)$$

These values are also recorded in Table 3.

The one-dimensional velocity dispersions found for clusters in our sample range from 0.8 to 2.8 km s⁻¹, with a mean of 1.8 km s⁻¹. For the ONC the *Gaia*-based velocity dispersion is $\sigma_{1D} = 1.8 \pm 0.1$ km s⁻¹. Estimates from earlier studies include ~ 2.3 km s⁻¹ from a proper-motion study by Jones & Walker (1988), 3.1 km s⁻¹ from an RV study by Fűrész et al. (2008), ~ 2.3 km s⁻¹ from an RV study by Tobin et al. (2009), ~ 2.5 km s⁻¹ from a RV study by Kounkel et al. (2016a), ~ 2.3 km s⁻¹ from a radio proper-motions study by Dzib et al. (2017), and 1.7 km s⁻¹ from an RV study by Da Rio et al. (2017) after corrections to take into account spatial variations in the mean velocity dispersion. Our value is smaller than most of these estimates, but approximately equal to the estimate by Da Rio et al. (2017). We note that our estimate is based only on the central cluster, rather than on larger areas that were the focuses of studies by Fűrész et al. (2008) and Kounkel et al. (2016a), for which the total velocity dispersions will include broadening effects from the velocity gradients identified by Da Rio et al. (2017).

There is a positive correlation between σ_{1D} and expansion velocity (Figure 11); Kendalls rank correlation test shows the dependence to be moderately statistically significant ($p = 0.01$). The one-dimensional velocity dispersions are significantly higher than the expansion velocities, mostly exceeding the bulk expansion velocities by a factor of 2–3. For cases where expansion rate varies with radius (e.g., Figure 7) this effect will contribute to velocity dispersions. For example, in a toy model with pure expansion from a central point, we would expect $\sigma_{1D} \approx 1.5 \bar{v}_{\text{out}}$. However, velocity dispersions that are

much larger than this imply that not all stars are moving outward.

In this initial *Gaia* study, the comparison of velocity dispersions in different regions comes with the caveat that the mass ranges of stars in the samples for different regions are not identical (e.g., Figure 1). If there is a relationship between a star’s mass and its velocity, then the selection of stars with good *Gaia* astrometry, which tend to be the brightest stars in a region, can affect the observed velocity dispersion. The clusters for which velocity dispersions are derived in Table 3 typically have samples that include stars with masses down to $0.5 M_{\odot}$.

In order to determine how sample selection may affect estimated velocity dispersions, we show plots of velocity versus absolute magnitude in the *J* band, where absolute magnitude is

$$M_J = J + 5 \log \varpi_0 [\text{mas}] - 10. \quad (18)$$

For the ONC and NGC 6530 we show the plots of both v_{α} and v_{δ} versus M_J in Figure 12. In both cases, for stars with $1 < M_J < 4$ mag (approximately a mass range of $0.5\text{--}2.5 M_{\odot}$; constituting the bulk of the sample) velocity dispersion stays relatively constant with magnitude.

There has been much interest, both observational and theoretical, of the effect of stellar mass on velocity dispersions in open clusters and globular clusters (e.g., Bianchini et al. 2016; Spera et al. 2016; Parker et al. 2016; Webb & Vesperini 2017; Bravi et al. 2018). Overall, studies suggest that open clusters do not achieve energy equipartition (cf. Spitzer 1969). We leave the full investigation of the kinematic implications of stellar mass and mass segregation in the *Gaia* DR2 data to a future study.

6. SUBCLUSTER MOTIONS

Many of the stellar complexes from the MYStIX and SFINC’s studies contain subclusters that have been delineated by Kuhn et al. (2014) and Getman et al. (2017). The clearest examples that have good *Gaia* data include NGC 2264, Cep OB3b, NGC 6530, the Rosette Nebula, NGC 6357, NGC 6611, and the Carina OB1 association. For this subset, we now examine the kinematics of the substructures relative to each other. Subclusters with insufficient *Gaia* data (<10 stars) are omitted.

Table 4 gives the properties of subclusters, including subcluster centers from earlier studies ² and the kinematics properties derived from *Gaia*. We find the bulk motions of subclusters by calculating the weighted median velocities of their stellar members. In a few cases, subclusters have been combined when overlapping

subclusters represent core–halo structures (Kuhn et al. 2017a). The projected subcluster velocities, relative to the association rest frame, range up to $\sim 8 \text{ km s}^{-1}$, with a median value of $\sim 2 \text{ km s}^{-1}$ and an interquartile range of $0.9\text{--}3.5 \text{ km s}^{-1}$. The velocity dispersions of subclusters can be quite different in different regions. The clusters in the Carina OB1 association have relative velocities of $5\text{--}8 \text{ km s}^{-1}$, while the various subclusters in NGC 2264 have relative velocities of $0\text{--}2 \text{ km s}^{-1}$.

Figure 13 shows spatial maps of the stars assigned to each subcluster along with the velocity vectors of each group. In general, the subcluster motions are not convergent, but appear either randomly oriented or divergent. This pattern is seen in almost every star-forming region investigated, ranging from well-delineated clusters in regions like NGC 6357 to clumpy distributions of stars in regions like NGC 2264. The main exception is in Carina where the motions of Tr 14 and Tr 16 are directed towards each other, but the apparent convergence of these clusters could be a chance alignment.

The contrast between internal cluster velocities and global kinematics of a complex can be clearly seen in the Carina OB1 association, which contains several clusters, including Tr 14/15/16 (included in this study) as well as Bochum 11 and the Treasure Chest to the south. Figure 14 (right) shows star positions in declination plotted against their v_{δ} velocity component. In this complex, the individual clusters are shifted with respect to one another in velocity, but internal velocity dispersions within the individual clusters can also be seen. In the south of the Carina OB1, there is a velocity gradient stretching from Bochum 11 to the Treasure Chest to Tr 16, while Tr 14 and Tr 15, to the north, have significantly different motions than the clusters to the south. Within Tr 14 and Tr 16, the positive correlation between declination and v_{δ} characteristic of an expanding cluster can be seen. The total velocity difference between different clusters is significantly larger than the velocity dispersions within the clusters. In contrast, in the lower-mass NGC 2264 region (left panel in Figure 14), small differences can be seen in the velocities of the different subgroups, but the magnitudes of these differences and the total velocity dispersions are much smaller.

We find no evidence for hierarchical assembly of rich clusters from subclusters in our sample. Evidence for this process would be converging motions of subclusters. This failure is expected, as *Gaia* does not provide access to the youngest embedded subclusters, but restricts our analysis to older clusters where the molecular cloud is at least partially dispersed. Thus, hierarchical cluster assembly, if it occurs, must occur promptly when a cluster is still embedded and must involve subclusters separated by $<5 \text{ pc}$ and ages $<1 \text{ Myr}$.

Subcluster motions are linked to the large-scale kinematics in molecular clouds, which may include effects of supersonic turbulence (Larson 1981; Mac Low & Klessen 2004; Padoan & Nordlund 2002; Krumholz & McKee

² In some case, the subcluster centers may not be perfectly centered among the stars seen by *Gaia*. This is an effect of differential absorption across a subcluster, limiting *Gaia*’s sensitivity in the high-extinction part.

2005), free-fall velocities of collapsing clouds (Vázquez-Semadeni et al. 2017), and/or accretion of material onto molecular clouds (Fukui et al. 2014; Ibáñez-Mejía et al. 2017). The clusters observed today at ages 1-5 Myr

were formed in different dense molecular cores at widely separated portions of a giant molecular clouds. It is therefore natural that they inherit the motion of their natal cloud cores, and exhibit spatially correlated but essential random motions with respect to each other.

Table 4. Relative Subcluster Kinematics

Region	Subcluster	α_0 (J2000)	δ_0 (J2000)	n_{samp} stars	$\langle v_\alpha \rangle$ km s ⁻¹	$\langle v_\delta \rangle$ km s ⁻¹
(1)	(2)	(3)	(4)	(5)	(6)	(7)
Rosette	A	6 30 57.1	+04 57 57	26	0.5±0.5	-1.2±0.7
—	C	6 31 32.0	+04 50 58	12	1.3±1.2	0.0±1.0
—	D+E	6 31 59.3	+04 54 50	241	0.5±0.3	0.5±0.3
—	H	6 33 7.2	+04 46 57	17	0.3±2.0	-0.8±0.5
—	L	6 34 10.7	+04 25 6	50	-0.5±0.4	-0.6±1.0
NGC 2264	D	6 40 45.8	+09 49 3	11	-0.7±0.2	-0.2±0.6
—	E	6 40 59.1	+09 52 22	67	-0.5±0.4	0.09±0.1
—	F	6 40 59.2	+09 53 59	10	-1.1±0.5	0.6±0.3
—	H	6 41 2.1	+09 48 44	16	-0.2±1.0	0.2±0.6
—	I	6 41 4.5	+09 35 57	13	1.7±0.7	0.4±0.2
—	J	6 41 6.3	+09 34 9	20	1.8±0.2	-0.4±1.0
—	K	6 41 8.2	+09 29 53	43	2.1±0.6	-0.7±0.4
—	M	6 41 14.9	+09 26 42	11	-0.5±0.8	-1.0±0.4
Carina	B+C	10 43 56.4	-59 32 54	262	-0.2±0.4	-1.9±0.2
—	D	10 44 32.9	-59 33 42	36	0.3±0.9	-2.9±0.9
—	E	10 44 34.0	-59 44 8	31	6.0±0.7	5.6±1.0
—	F	10 44 37.4	-59 26 3	34	-1.0±0.9	-0.9±0.8
—	H	10 44 41.8	-59 22 5	59	-5.2±0.7	-2.3±0.6
—	I	10 44 45.3	-59 20 7	24	-4.9±0.4	-1.4±1.4
—	J	10 45 2.4	-59 45 50	41	4.5±1.1	4.9±0.7
—	K	10 45 6.2	-59 40 21	30	4.4±0.5	6.0±0.5
—	L	10 45 11.1	-59 42 46	51	3.4±0.3	4.5±0.6
—	M	10 45 13.7	-59 57 58	23	2.3±1.3	1.0±1.0
—	O	10 45 53.4	-59 56 53	11	0.9±1	-1.3±0.7
—	P	10 45 54.4	-60 04 32	47	-0.2±1.6	-3.2±1.3
—	Q	10 45 55.2	-59 59 51	23	-0.1±1.0	1.3±1.1
—	R	10 46 5.4	-59 50 9	19	-1±1	1.7±0.9
—	S	10 46 52.7	-60 04 40	13	-2.8±0.7	-4.6±1.5
—	T	10 47 12.5	-60 05 58	33	-3.1±0.6	-3.7±0.8

Table 4 continued

Table 4 (*continued*)

Region	Subcluster	α_0	δ_0	n_{samp}	$\langle v_\alpha \rangle$	$\langle v_\delta \rangle$
		(J2000)	(J2000)	stars	km s ⁻¹	km s ⁻¹
(1)	(2)	(3)	(4)	(5)	(6)	(7)
NGC 6357	A	17 24 43.7	-34 12 7	34	-1.1±0.5	3.1±0.5
—	B	17 24 46.7	-34 15 23	23	-1.6±0.9	1.3±0.7
—	C+D	17 25 34.3	-34 23 10	27	1.0±0.6	2.4±1.2
—	E	17 25 47.9	-34 27 12	11	-4.1±2.1	-2.7±0.8
—	F	17 26 2.2	-34 16 42	21	1.8±1.1	-1.0±0.8
NGC 6530	A	18 3 23.8	-24 15 19	15	-3.4±1.2	1.9±0.8
—	C	18 3 46.3	-24 22 1	14	2.2±3.3	-1.9±0.9
—	D	18 3 51.3	-24 21 8	11	4.1±2.1	-1.1±0.8
—	E	18 4 7.6	-24 25 53	55	-0.9±1.1	-1.8±0.5
—	F	18 4 13.3	-24 18 27	173	1.5±0.4	1.1±0.3
—	G	18 4 20.1	-24 22 51	14	0.6±1.0	0.6±1.0
—	H	18 4 23.3	-24 21 13	65	0.03±0.4	0.8±0.2
—	I	18 4 28.3	-24 22 46	110	0.3±0.2	-0.5±0.5
—	J	18 4 39.6	-24 23 20	31	-0.7±0.5	0.04±0.3
—	K	18 4 50.5	-24 26 19	45	-2.3±0.9	-0.1±0.8
NGC 6611	A+B	18 18 42.2	-13 47 3	213	0.5±0.3	-0.1±0.3
—	D	18 18 57.3	-13 45 23	71	-1.7±0.4	0.9±0.7
Cep OB3b	A	22 53 47.1	+62 35 47	195	2.2±0.4	-0.9±0.4
—	B	22 54 58.4	+62 34 9	23	-0.1±0.5	-0.5±0.4
—	C	22 56 40.3	+62 42 6	401	-0.6±0.3	0.2±0.3

NOTE—Column 1: The names of the star-forming regions. Column 2: The names of the subclusters defined by [Kuhn et al. \(2014\)](#) and [Getman et al. \(2018a\)](#). Columns 3–4: Coordinates of the subcluster centers. Column 5: The number of *Gaia* sources in each subcluster. Column 6–7: Subcluster velocity projected in the plane of the sky relative to the center-of-mass rest frame of the entire association.

7. RELATIONSHIPS BETWEEN KINEMATICS AND OTHER CLUSTER PROPERTIES

Physical cluster properties, such as cluster mass, size, and age can be linked to internal cluster kinematics. These links may arise from cluster dynamics or through the cluster formation process. For example, the relationship between cloud size and cloud velocity dispersion ([Larson 1981](#)) could yield a relationship between a cluster mass and cluster velocity dispersion.

We have obtained characteristic cluster masses, sizes, and ages based on previous analysis of MYS-tIX/SFInCS/NGC6231 datasets, applying corrections for the updated distances from *Gaia*. Spatial distributions of stellar mass (corrected for incompleteness) were calculated using the methods from [Kuhn et al.](#)

(2015b) and median ages for clusters were calculated using the *Age_{JX}* method from [Getman et al. \(2014\)](#). Nevertheless, systematic effects, such as choice of model isochrones and inference of stellar properties, may affect these measurements ([Richert et al. 2018](#)). Furthermore, M_{cl} and r_{hm} could be underestimated due to difficulties determining the outer boundaries of clusters and the finite fields of view in the MYS-tIX/SFInCS/NGC6231 studies.³ Even though the molecular cloud complexes are only partially covered by our fields of view ([Kuhn et al. 2015b](#), their Figure 5), in most cases the main clusters that are the focus of this study lie (almost) entirely within the fields of view. In the *Chandra* studies

³ See [Kuhn et al. \(2017a\)](#) for a detailed discussion of challenges involved in obtaining M_{cl} and r_{hm} .

of both the ONC and NGC 6231, some vignetting of the main clusters does occur. These considerations make it difficult to establish formal uncertainties on M_{cl} , r_{hm} , and cluster age.

Figure 15 shows the values of M_{cl} , r_{hm} , and age, plotted against σ_{1D} and median v_{out} . Statistically significant correlations are found between σ_{1D} , M_{cl} , and r_{hm} using Kendall's rank correlation test ($p < 0.01$), while expansion velocities show no statistical correlation with any of the measured cluster properties. As mass and radius are themselves related to each other, multivariate regression analysis is needed to treat interdependencies. Using the R function lm to perform linear regressions with $\log \sigma_{1D}$ and median v_{out} as response variables, we obtain

$$\log \sigma_{1D} = a + b_1 \log M_{cl} + b_2 \log r_{hm} + b_3 \log \text{age}, \quad (19)$$

where $a = 0.46 \pm 1.31$, $b_1 = 0.15 \pm 0.06$, $b_2 = 0.17 \pm 0.16$, and $b_3 = -0.12 \pm 0.20$. Analysis of this regression using the *relaimpo* package in R (Grömping et al. 2006) shows that $\log M_{cl}$ is the only important predictor of σ_{1D} . A similar analysis for expansion velocity revealed no statistically significant predictor of expansion. Although the relationship between cluster mass and velocity dispersion was expected, the result is interesting because it provides empirical evidence for the relationship based on independent estimates of cluster masses and velocity dispersions.

The cluster crossing time, defined as $t_{cross} = 2r_{hm}/\sigma_{1D}$, and the ratio of cluster age to crossing time are two additional quantities that are important to cluster dynamics (Binney & Tremaine 2008). Crossing times range from 0.4 to 3 Myr in our sample, while the ratios of cluster age to crossing time range from 0.6 to 3. This indicates that the clusters are all dynamically very young, and would not have had time to relax through two-body interactions. Cluster expansion can also drive the ratio of age to crossing time toward a small value, if a cluster expands at a rate proportional to its velocity dispersion. Surprisingly, there is no statistically significant correlation between either of these quantities and either velocity dispersion or expansion rate for the objects in our sample (Figure 15).

7.1. Virial State

The observed velocity dispersion of a cluster can be compared to the velocity dispersion needed for virial equilibrium σ_{virial} to estimate whether a cluster is subvirial, virial, supervirial, or unbound. Given a mass M_{cl} and half-mass radius r_{hm} , the velocity dispersion of a virialized cluster would be

$$\sigma_{virial} = \left(\frac{G M_{cl}}{\eta r_{hm}} \right)^{1/2}, \quad (20)$$

where G is the gravitational constant and η is a constant that depends on the mass profile of a cluster. A

Plummer model yields $\eta \approx 10$, which we adopt here. If $\sigma_{1D} > \sqrt{2}\sigma_{virial}$, the total energy of the cluster would be positive and the system would be unbound.

Figure 16 shows σ_{1D} vs. σ_{virial} . There is a clear positive correlation between these two quantities. All clusters lie above the solid line showing the relationship for virial equilibrium, and most clusters lie above the dashed line showing the limit for a bound system, suggesting that most clusters are unbound. Nevertheless, the calculated statistical uncertainties on velocity dispersion or the unknown systematic uncertainties on mass and radius could allow several additional clusters to be gravitationally bound. We have highlighted several non-expanding clusters (ONC, NGC 6231, and NGC 2362) and two clusters with clear expansion (NGC 6530 and Cep B). The non-expanding clusters lie at the bottom of the distribution, while the expanding clusters lie toward the top, as would be expected if expansion is driven by clusters being unbound. The ONC is within the region considered gravitationally bound, and NGC 6231 and NGC 2362 could be within this region given measurement uncertainties.

7.2. Dynamical State of Non-Expanding Clusters

If a cluster is in virial equilibrium, its radial density profile is expected to be linked to its kinematic properties. Here we examine three clusters, the ONC, NGC 6231, and NGC 2362, which do not show significant expansion and are the best candidates for being gravitationally bound.

The core radius r_c – the radius where the apparent surface-density of stars drops by a factor of ~ 2 – can serve as a length scale with which to connect the spatial and kinematic cluster properties. For a dynamically relaxed cluster, with a surface density profile given by a King profile or an isothermal sphere, the density at the center of the clusters, ρ_0 , is related to the cluster core radius, r_c , and the velocity dispersion, σ_{1D} , by the equation

$$\rho_{0,virial} = \frac{9\sigma_{1D}^2}{4\pi G r_c^2}, \quad (21)$$

where G is the gravitational constant (Binney & Tremaine 2008). For clusters in which the potential is dominated by the stars (versus needing to account for $M_{stars} + M_{gas}$), the mass density implied by the cluster dynamics can be compared to the observed cluster number density n_0 , to infer the mean mass per star. This, in turn, can be compared to the average mass per star predicted by a standard initial mass function (IMF). Adopting the Maschberger (2013) form of the IMF over the mass range 0.08–150 M_\odot yields $\bar{m} = 0.61 M_\odot$ for single stars or $\bar{m} = 0.78 M_\odot$ assuming a population including unresolved binary systems.

The ONC is a smooth, centrally concentrated distribution of stars, which was modeled by Hillenbrand & Hartmann (1998) using a King profile (King 1966; Binney &

Tremaine 2008) with a core radius of $\sim 0.15\text{--}0.20$ pc.⁴ Although the cluster is located within the Orion A Cloud, the central region of the cluster is dominated by stars, not dense gas; an ionization front propagates back into the molecular cloud, located approximately 0.2 pc behind the cluster center, and a neutral gas “lid” is located >1 pc in the foreground (O’dell 2001). Hillenbrand & Hartmann (1998) used velocity measurements from Jones & Walker (1988) to compare the virial central density of the ONC to the observed number density of stars. We repeat this experiment, instead using the $\sigma_{1D} = 1.8$ km s⁻¹ from *Gaia* measurements and scaling their core radius to $r_c = 0.14$ pc and their observed density of stars to $n_0 = 2.7 \times 10^4$ stars pc⁻³ based on differences in distance assumptions. This gives $\rho = 2.8 \times 10^4 M_\odot \text{pc}^{-3} = 1.0 M_\odot n_0$. A value of $1.0 M_\odot$ per star is slightly higher than the expected mean stellar mass, but some of the virial mass may be made up by accounting for some amount of remaining gas in the outer parts of the cluster. Thus, the ONC is close to virial equilibrium.

NGC 6231 and NGC 2362 are both larger, older, and less dense than the ONC. The large sizes suggest that they may have already expanded, but may have reached a turn-around radius where outward expansion has halted.

For NGC 6231, values of $r_c = 1.3$ pc and $n_0 = 180$ stars pc⁻³ were found by Kuhn et al. (2017a), scaled for difference in assumed distances.⁵ A velocity dispersion of $\sigma = 1.7$ km s⁻¹ values yield $\rho_{0,\text{virial}} = 270 M_\odot \text{pc}^{-3} = 1.5 M_\odot n_0$, a slightly larger ratio than for the ONC. In this case, the cluster is completely devoid of molecular cloud, so gas mass cannot contribute significantly to the total mass. Assuming the average mass per star (or binary) is $\sim 0.6\text{--}0.8 M_\odot$ this would place NGC 6231 near the threshold for being unbound, but whether the cluster is bound or unbound depends on the total mass of the cluster.

For NGC 2362, values of $r_c = 0.36$ and $n_0 = 600$ stars pc⁻³ were found by Kuhn et al. (2015a),

⁴ The structure of the ONC core is more complex than accounted for by a single King profile. For example, there are small concentrations of stars with densities much greater than accounted for by the smooth King model (e.g., Henney & Arthur 1998; Rivilla et al. 2013; Kuhn et al. 2014). We use the simpler model form from Hillenbrand & Hartmann (1998) because it is easier to interpret dynamically.

⁵ The estimation of the number of stars in the cluster (on which n_0 depends linearly) is based on extrapolation of the IMF to account for incompleteness in the observation and, thus, depends on assumptions of stellar age, pre-main-sequence isochrones, cluster distance, and the shape of the IMF. Kuhn et al. (2017a) estimated a total of 5700 stars down to $0.08 M_\odot$ projected within the field of view, while Damiani et al. (2016) estimated a similar cluster mass using different assumptions.

scaled for difference in distance.⁶ A velocity dispersion of $\sigma = 0.83$ km s⁻¹ yields $\rho_{0,\text{virial}} = 870 M_\odot \text{pc}^{-3} = 1.5 M_\odot n_0$. NGC 2362 is also a region from which gas has been expelled, so again the molecular cloud cannot provide the additional mass. However, uncertainty in mass estimation could make the difference between a bound and unbound cluster.

Cluster structure will also affect how velocity varies as a function of radius, assuming that a cluster is close to virial equilibrium. For the isothermal sphere, velocity dispersion is independent of position throughout the cluster. However, other plausible distribution functions, including the Plummer sphere and the lowered isothermal sphere models (also known as King models), have velocity dispersions that decrease monotonically with radius (Binney & Tremaine 2008). In Plummer spheres the velocity dispersion at a point at radius r is proportional to $(1 + r/r_c)^{-1/4}$. The family of King models is characterized by a parameter W_0 describing the central potential (King 1966), and curves of one-dimensional velocity dispersion as a function of projected radius are shown by Binney & Tremaine (2008, their Figure 4.11) for several values of W_0 .

Figure 17 shows velocity dispersion dependence on radius for the ONC, NGC 6231, and NGC 2362. For the ONC and NGC 2362 velocity is nearly constant out to a radius of 8 times r_c , while for NGC 6231 it decreases steeply with radius (by a factor of ~ 2 at a distance of $4 r_c$ from the center). For the ONC and NGC 2362, these velocity profiles would be consistent with isothermal spheres or King models with $W_0 \geq 9$. However, the Plummer model is rejected. For NGC 6231, the velocity dispersion is consistent with the Plummer model or King models with $3 < W_0 < 6$. In all three cases, the youth of the systems means that there has been insufficient time for clusters to become dynamically relaxed via two-body interactions.

7.3. Dynamical State of Expanding Systems

The two examples with the most statistically significant expansion are NGC 6530 and Cep B, both of which have “Hubble flow” like expansion patterns (Figure 7) which hint at free expansion. They have one-dimensional velocity dispersions of 2.2 ± 0.2 km s⁻¹ and 1.9 ± 0.2 km s⁻¹ and approximate half-mass radii of ~ 2 pc and ~ 1.5 pc, respectively. For these values and the assumptions above, NGC 6530’s virial mass would be $\sim 20,000 M_\odot$ and Cep B’s virial mass would be $\sim 10,000 M_\odot$. However, the estimated cluster masses are only $\sim 4000 M_\odot$ and $\sim 1000 M_\odot$ (Kuhn et al. 2015b). Thus, both the gradient in expansion velocity and the inferred stellar populations indicate that these two clus-

⁶ As for NGC 6231, the estimated density of stars at the center of NGC 2362 depends on model-based corrections for incompleteness in the observed sample.

ters are not gravitationally bound. This places these expanding associations near the top of the distribution on Figure 16.

For a freely expanding association, stars will sort themselves by velocity as they move away from the center of the cluster, effectively decreasing the local velocity dispersion. This can be tested in NGC 6530 by plotting the ratio of expansion velocity to the dispersion in v_{out} as a function of radius (Figure 18). Values of this ratio >1 suggest that nearly all stars are moving outwards, while values <1 suggest some stars are moving inwards even as the cluster expands overall. In this case, it turns out that the expansion velocity is always less than or equal to the local velocity dispersion.

Many of the expanding clusters show internal substructure (Kuhn et al. 2014). We have not analyzed the kinematics within individual subclusters due to insufficient numbers of stars in our sample. In principal, it would be possible for subgroups of stars to be locally bound, even if the total energy of a region as a whole is positive. Future *Gaia* data releases are likely to provide more information about these groups due to larger samples of stars with good astrometry and higher overall precision.

8. DISCUSSION

The *Gaia* data reveal considerable diversity in kinematic properties in our sample of nearby young clusters, with examples of both expanding and non-expanding systems (Figures 2–6). The expected pattern of increased expansion velocity with distance from the cluster center is seen (Figure 7). Velocity dispersions range from 1 to 3 km s⁻¹, exhibit Gaussian distributions, and often exceed the expectations of virial equilibrium (Figures 9–11, 16).

On larger scales, we examine the relative motions of subclusters in star forming complexes. Subcluster trajectories are typically divergent, reflecting their origins in turbulent clouds, rather than convergent as expected if clusters are currently assembling from smaller components (Figure 13).

8.1. Expectations from Simulations

Theoretical models of star cluster formation, informed by hydrodynamical and N -body codes, have led to predictions about the stellar dynamics of very young clusters – even before sufficiently precise kinematic data were available to test these models.

Cluster simulations typically show an initial collapse during the first crossing time where the global contraction is accompanied by increasing velocity dispersion. This brief phase is followed by a re-expansion with outward velocity accompanied by a slight decrease in velocity dispersion (e.g., Proszkow et al. 2009, their Figure 1). Departure from spherical symmetry, such as elongated clusters, will produce observed kinematic structure dependent on viewing angle. These projection effects can

produce apparent velocity gradients and can influence the velocity dispersion by about a factor of two, mostly during the expansion phase (Proszkow et al. 2009).

In gas-rich environments, subclusters are likely to merge into more massive young star clusters (Fellhauer et al. 2009; Maschberger et al. 2010). Kuznetsova et al. (2015a) find that the gas potential dominates on time scales $< 0.75 - 1 \times \tau_{\text{freefall}}$, encompassing the initial infall and star formation phases. By the time the stellar potential begins to dominate, subclusters have already merged. Kuznetsova et al. (2015a) report stellar velocity dispersions of 3-4 kms⁻¹ compared to gas velocity dispersion of 1-2 kms⁻¹ for an isothermal (cold, sub-virial) model of an ONC-like cluster. Other simulations (Banerjee & Kroupa 2018) imply that some observed massive young star clusters are too compact to be produced through hierarchical formation, thus suggesting the monolithic formation route.

At the more advanced age at which young clusters are revealed in optical wavelengths, their initial kinematic state will have been influenced by any previous merging, and they should be a state of global expansion, on their way to virial equilibrium (Parker & Wright 2016). Only the youngest, embedded clusters can be caught during the infall or near the turnaround phase of cluster evolution.

In the following discussion (Sections 8.2-8.4), we use a simulation of cluster assembly from Sills et al. (2018) as a benchmark to compare with the observed clusters in our study. The model used for comparison is the “DR 21 Fiducial Model” designed to understand the current gas and stellar distribution in DR 21, a massive filamentary star-forming region in the Cygnus X region. A full description of the model’s initial conditions and assumptions is given by Sills et al. (2018). Briefly, this is a simulation of a 3000 M_{\odot} star cluster in which stars originate in a chain of subclusters, spatially dispersed following the pattern of observed stars in DR 21. Each subcluster is modeled with an elongated Plummer sphere and a velocity dispersion based on the virial parameter. The subclusters have no initial bulk motion relative to each other in this simulation. Gas was modeled without star formation or stellar feedback, and moves gently out of the cluster center during the simulation. The model simulates the first 10 Myr of dynamical evolution, showing the progression from a clumpy assembly of subclusters to a single, virialized massive young star cluster.

8.2. Cluster Assembly

The clusters included in our *Gaia*-based study are typically several million years old, and the clouds from which stars are forming have been partially or completely dispersed, so the epoch of cluster assembly will have mostly finished. However, the kinematic properties such as cluster rotation and the motions of subclusters can provide constraints on how clusters were assembled.

Our data shows no evidence for ongoing cluster mergers. This implies that hierarchical cluster assembly, if it takes place, must occur early-on while star-formation is still most active.

In the simulation from Sills et al. (2018), starting at an earlier stage of evolution, subclusters rapidly converge to form a single cluster in ~ 1 Myr. The evolution of the median v_{out} and velocity dispersion, calculated in the same way as above for the real clusters, is shown for the first 10 Myr in Figure 19. The infall of subclusters produces an initial negative median v_{out} for the central cluster for the first 2 Myr. The velocity distribution rebounds, yielding cluster expansion, before settling into a quasi-static state at ~ 6 Myr. The infall velocity reaches -0.75 km s^{-1} , while the rebound outward velocity peaks at $\sim 0.5 \text{ km s}^{-1}$. The velocity dispersion increases during infall, peaking at the point of rebound, then settling down to just under 2 km s^{-1} .

The only cluster in our study that may be caught in a phase of initial collapse is M 17, which appears to have a large (though uncertain) contraction velocity (median $v_{\text{out}} = -2.5 \pm 1.3 \text{ km s}^{-1}$). The spatial structure of stars in M 17 is also distinctive, being one of the few clusters in the MYStIX survey with a “clumpy” structure suggesting that the merging of many subclusters is still underway (Kuhn et al. 2014). However, the other embedded clusters do not appear to be undergoing such rapid collapse. The regions NGC 1333 and NGC 2264 IRS1/2, much less massive than M17, are also gas rich and contain protostars. These regions have neither statistically significant expansion nor contraction.

For clusters and associations in more evolved star-forming regions, where molecular gas has been partially or fully dispersed, the motions of subclusters are inconsistent with mergers. This supports the theoretical prediction that hierarchical cluster assembly, if it occurs, must happen promptly before gas is expelled by stellar feedback.

Rotational properties of young star clusters can also be used to test the hierarchical assembly scenario. Simulations of star formation by Mapelli (2017) indicate that bulk rotation should be common for clusters at ages of 1-2 Myr due to large-scale torques imparted on the gas as cluster assembly occurs. Lee & Hennebelle (2016) also highlight the prominence of cluster rotation, which in their simulations results naturally from conservation of angular momentum during the global collapse. Here rotation accounts for approximately 1/3 of the total kinetic energy, and together with turbulence acts to counteract gravity to keep the cluster globally virialized. In both the Mapelli and Lee & Hennebelle models, rotation signatures should be stronger than expansion signatures. We do not confirm this result here, presenting an important constraint on the physical processes of cluster assembly.

8.3. Bound Clusters

Our study may include several systems that will survive (temporarily) as bound open clusters. The best candidates are the ONC, NGC 6231, and NGC 2362. These clusters are not currently expanding at a significant rate, and have total energies near the division between bound and unbound systems. The ONC is still quite compact, while NGC 6231 and NGC 2362 have already expanded. Despite the young ages of these clusters, which are all less than their virialization timescales for two-body interactions, they all show properties that would be expected for virialized systems. They are relatively well-fit by cluster models, and the cluster density, cluster core radius, and velocity distributions are consistent with theoretical expectations given the uncertainties. Velocity dispersions in these clusters are Gaussian, constant with radius (expected for an isothermal structure) or decreasing.

In our sample, the ONC provides the best cases for modeling velocity dispersions. For an isothermal sphere with equal-mass stars, the distribution of stellar velocities will be Maxwellian (i.e. a multivariate normal distribution) given by,

$$p(v_x, v_y, v_z) \propto \exp\left(-\frac{\bar{m}(v_x^2 + v_y^2 + v_z^2)}{2kT}\right), \quad (22)$$

where $T = \bar{m}\sigma_{1D}^2/k$ is a characteristic temperature of the system. Due to a number of assumptions that are violated in real young star clusters, there is no reason to expect *a priori* that this distribution should accurately describe stellar velocities. Nevertheless, it turns out that the stars in the ONC are well described by a multivariate normal (Figure 10), but the distribution is elongated north-south (Figure 9). The elongation is parallel to the orientation of the Orion A cloud, so it could result from perturbations of the gravitational potential from asymmetry in the star-forming complex, or it could be a residual effect of the cluster formation from a molecular filament (e.g., Proszkow et al. 2009; Kuznetsova et al. 2015b).

The properties of clusters like the ONC, NGC 6231, and NGC 2362 that are likely bound can be compared to the simulated cluster from Sills et al. (2018) to test the accuracy of its predictions. For several time points from the simulation, Figure 20 shows stellar velocity v_{out} as a function of projected radius R . For each evolutionary stage shown, velocity dispersions are higher in the cluster center and lower in the cluster periphery. This is also clearly seen in Figure 19, where velocity dispersions are strongly affected by distance from the center of the cluster. This pattern is similar to radial dependence of velocity dispersion found in NGC 6231 (Figure 17), but is different from the isothermal distributions in the ONC and NGC 2362. Future simulations can be used to test which initial conditions can produce the different types of observed velocity profile.

8.4. Expanding Associations

Most of the regions included in our study contain stellar populations that are unbound and are expanding (Figure 16). The conditions of formation of large OB associations like Sco-Cen has been uncertain, with debate about whether these were produced by expansion of an association or widely distributed star-formation events (Wright et al. 2016; Wright & Mamajek 2018; Ward & Kruijssen 2018). The clusters in our sample are currently fairly compact, with sizes of several parsecs, but their kinematic properties mean that they will inevitably grow to sizes larger than 100 parsecs across.

NGC 6530 may be a good analog of a precursors to a massive OB association. The bulk expansion velocity of NGC 6530 is 0.9 km s^{-1} , but its velocity dispersion is 2.2 km s^{-1} . The mass of the cluster compared to its virial mass is sufficiently low that self-gravity will have little effect on the evolution of stellar velocities, and the association will expand ballistically. In 10 Myr, a star traveling at 2.2 km s^{-1} will travel 22 pc while a star with a velocity of 4.5 km s^{-1} (2σ from the mean) would travel 45 pc, so that $\sim 95\%$ of the stars would be found within an region with a length of ~ 90 pc. This size is quite similar to the size of Upper Scorpius in the Scorpius-Centaurus Association, which is $\sim 75\text{--}100$ pc long along its longest axis (Galli et al. 2018) and has an age of ~ 10 Myr (Pecaut & Mamajek 2016). The estimated mass for NGC 6530 of $\sim 4000 M_{\odot}$ is somewhat higher than $1400 M_{\odot}$ for Upper Scorpius (Preibisch & Mamajek 2008).

For the simulated cluster of Sills et al. (2018), the median v_{out} (Figure 19) expands after initial contraction, reaching an expansion speed of $\sim 0.5 \text{ km s}^{-1}$, similar to the typical value observed for our expanding clusters (Figures 6 and 11). Velocity dispersion is also near maximum at this time, with a value of 2.5 km s^{-1} . We also note that at the point of maximum expansion velocity in the simulation at ~ 2.5 Myr, expansion velocity increases with radial distance from the cluster center (Figure 19, left), similar to the trends seen in Figure 7 for NGC 6530 and Cep B. However, the rebound expansion in the simulation is unlikely to explain the expansion we have observed in many clusters, given that the simulated cluster settles down into a quasi-equilibrium state after 6 Myr, while unbound clusters will keep expanding.

The lack of unbound expansion of the simulated clusters suggests that an additional mechanism, not included in the simulation, is necessary to disrupt massive star-forming regions like NGC 6530. For example, gas expulsion from stellar feedback (which was omitted in this simulation) may enhance cluster disruption. We note that the two low-mass clusters NGC 1333 and IC 348, which do not have O and early-B stars that could produce rapid gas expulsion, do not exhibit significant expansion.

9. CONCLUSIONS

The superb astrometric measurements of the *Gaia* spacecraft provided in DR2 have allowed us to examine the kinematics of nearby young star clusters including many of the most massive star-forming complexes in our neighborhood of the Galaxy. The study also makes use of large samples of YSOs in these regions from the MYStIX and SFiNCs projects. Results from our sample of 28 clusters and associations likely represent the environments in which most star formation takes place in mature spiral galaxies.

The main scientific results of this study are:

1. Bulk expansion is commonly seen for young star clusters during the first few million years. 70% of the clusters in the sample have positive expansion velocities, and expansion velocities range up to 2 km s^{-1} , with a median value of $\sim 0.5 \text{ km s}^{-1}$. Significant expansion around 1 km s^{-1} is measured for NGC 6530 in the Lagoon Nebula, Cep B in the Cep OB3b association, Tr 16 in the Carina Nebula, NGC 2244 in the Rosette Nebula, NGC 6611 in the Eagle Nebula, and NGC 1893.
2. The most rapidly expanding clusters have positive total energies, so their expansion can be explained as cluster dispersal. Velocity dispersions are sufficiently large for these associations to expand to the size of well-known OB associations like Sco-Cen in ~ 10 Myr.
3. A positive radial gradient in expansion velocity is seen in some expanding systems like NGC 6530, Cep B, NGC 2244, and Tr 16. Radial gradients in velocity can result from faster stars traveling larger distances, which yields positional sorting of stars by velocity. This phenomenon would be most prominent in systems where stellar trajectories are affected little by the gravitation of the cluster, so detection of this gradient provides evidence that these regions are unbound associations. In contrast, in a simulation of expansion in a gravitationally bound cluster, no radial dependence is seen.
4. Several clusters show no evidence for expansion. Notable in this group is the still-compact ONC and the larger clusters NGC 6231 and NGC 2362 that may have expanded in the past. All three have velocity dispersions consistent with virial equilibrium; the ONC and NGC 2362 have isothermal velocity distributions while velocity dispersion decreases with radius in NGC 6231. The velocity dispersion in the ONC is approximately Gaussian. These findings are consistent with predictions of bound cluster models, and we expect that these clusters will emerge as gravitationally bound, main sequence, open clusters.

5. The cluster M17 is unique in showing evidence (2σ significance) of contraction with velocity $\sim 2.5 \text{ km s}^{-1}$. This is consistent with its clumpy stellar structure and suggests it is still in the process of assembly. NGC 1333 and IC 348 in the Perseus cloud, still embedded in their clouds with protostars, do not show signs of expansion or contraction.
6. There is no evidence for cluster rotation in all but one case, Tr 15. Theoretical simulations indicate that rotation is expected to be present in clusters that inherit angular momentum from the merging of large subclusters, so its absence provides constraints on cluster formation. More sensitive measurements are required to further constrain rotation of young clusters.
7. In the cluster sample, one dimensional velocity dispersions, σ_{1D} , range from 1 to 3 km s^{-1} . The velocity dispersion for the ONC ($1.8 \pm 0.13 \text{ km s}^{-1}$) is slightly lower than most previous estimates based on radial velocity studies. In the full cluster sam-

ple, velocity dispersions are typically greater than bulk expansion velocities by a factor of $\sim 2\text{--}3$.

8. The relative motions of clusters within a massive star forming regions generally show random motions, likely inherited from the parent molecular clouds. They do not generally have convergent motions expected from hierarchical assembly, indicating that any cluster merging occurred during an embedded phase before the clusters were observed.

While indirect evidence of cluster dispersal had been claimed previously (e.g., Pfalzner 2009), the *Gaia* observations provide direct evidence that stars produced in compact massive star-forming regions are more likely to immediately disperse after gas expulsion. Only a few pre-main-sequence clusters are likely to produce gravitationally bound, main sequence, open clusters. Future *Gaia* data releases are anticipated to dramatically improve astrometry for fainter sources, which will allow kinematics studies of stellar populations with higher absorption than the ones included in this study. This will improve constraints on processes of cluster assembly and help distinguish which star-formation environments produce clusters of different dynamical fates.

APPENDIX

A. DISTANCE TO ORION

The Orion region is sufficiently close that distance measurements differ slightly depending on the location in the cloud. Based on our weighted median method described in the body of the paper, we find a median parallax of $\varpi = 2.482 \pm 0.041$ for the X-ray selected probable cluster members in the ONC *Chandra* Field, corresponding to a distance of 403 pc. This field includes the dense central cluster, also known as the Trapezium Cluster, but excludes stars associated with Orion A that lie more than 1.5 pc from the center. Kounkel et al. (2018) report a *Gaia*-derived distance of 386 ± 3 pc for the ONC, which is based on a much larger region spanning $\delta = -7^\circ$ to -4° in declination. Their analysis also differs in that they apply a correction to the *Gaia* parallaxes to account for systematic differences between astrometry from *Gaia* and the VLBA based on Kounkel et al. (2016b). This correction shifts objects at the distance of the ONC nearer by ~ 10 pc. In our work, we have not applied this correction.

Figure 21 shows *Gaia* parallax measurements as a function of declination in the Orion A cloud. We fit a non-parametric *loess* curve (Cleveland 1979) and compute 95% confidence intervals, which reveals some variation in mean parallax for stars in different parts of the Orion A complex. The ONC itself is recessed (403 pc), while the stars to the north and south (including populations of stars both embedded in the filament and outside it) are nearer (395 pc). Given that this study is focused on the kinematics of the main cluster, we use the 403 pc distance. However, the discrepancy between our value and the distance from Kounkel et al. (2018) can be explained by a combination of the different sizes of the region analyzed and whether additional correction factors are applied to *Gaia* astrometry.

B. PROPER MOTION CORRECTIONS DUE TO RVs

Calculating the contribution of perspective expansion to proper motions in Equations 1 and 2 requires measurements of the RVs of clusters. We have compiled a list of RVs for the clusters (Table 5) based on both previously published RV measurements and RV measurements made by the *Gaia* spacecraft (Cropper et al. 2018). There are a few cases of discrepancies in RVs from the literature and/or median RVs from *Gaia*. In order to assign RV measurements to all clusters so that proper-motion corrections can be computed, we favor 1) the median *Gaia* RV when at least 5 stars are available, 2) the most recent literature RV, and finally 3) the *Gaia* RVs based on 1–4 stars. For Tr 15, which lacks its own independent RV measurement, we assign it an RV of -20 km s^{-1} based on the motion of the Carina Nebula as a whole.

Table 5. RVs of clusters

Region	Sample	RV_{Gaia} km s ⁻¹	RV_{lit} km s ⁻¹
Berkeley 59	0	...	-14.5 ^a , -6.50 ^b
NGC 1333	0	...	8.02 ^c
IC 348	8	19.7±2.2	14.00 ^b , 15.37 ^d
LkHα 101	2	5.74±3	11–13 ^{e*}
NGC 1893	0	...	-2.25 ^b
Orion A Cloud			
— ONC	12	21.8±6.6	26 ^f , 28.94 ^b
— OMC 2–3	9	22.6±5.5	
— Orion Flank S	5	25.2±4.8	
— Orion Flank N	7	27.4±3.3	
Mon R2	1	35.6±3	28 ^g
NGC 2244	1	19.1±0.96	26.16 ^b
NGC 2264	7	15.8±2.9	22 ^h , 17.68 ^b
NGC 2362	1	28.9±5.7	25.33 ^b
Carina			
— Tr 14	0	...	-6.7 ⁱ , -15.0 ^b
— Tr 15	0
— Tr 16	0	...	-25.00 ^b
NGC 6231	1	-19.1±1	-27.28 ^b
RCW 120	1	13±4.1	-16 ^{j*}
NGC 6357	0	...	-12 ^{k*}
M20	0	...	-2.13 ^b
NGC 6530	0	...	-13.32 ^b
NGC 6611	3	16:	18.00 ^b , 10 ^l
M17	0	...	-17.00 ^b
IC 5146	1	4.59±10	-5.5 ^m , ~5 ⁿ
NGC 7160	1	-28±8.1	-23.8 ^m , -26.28 ^b
Cep OB3b	4	-28.7±4.4	-22 ^o , -15.12 ^b

NOTE—Column 1: Region name. Column 2: Number of members with *Gaia* RV measurements. Column 3: Median RV (barycentric). Column 4: RV measurements from the literature (barycentric). Measurements for cloud gas are marked with an asterisk.

RV references: (^a) Liu et al. (1989), (^b) Kharchenko et al. (2005), (^c) Foster et al. (2015), (^d) Cottaar et al. (2015), (^e) Dewdney & Roger (1982), (^f) Fűrész et al. (2008), (^g) Kim et al. (2004), (^h) Fűrész et al. (2006), (ⁱ) Dias et al. (2002), (^j) Blitz et al. (1982), (^k) Caswell & Haynes (1987), (^l) Evans et al. (2005), (^m) Liu et al. (1989), (ⁿ) Liu et al. (1991), (^o) Pozzo et al. (2003).

We thank Alberto Krone-Martins for providing us with his expert knowledge about *Gaia*, Floor van Leeuwen for advice about astrometry, and Anushree Sengupta for useful feedback on the article. E.D.F. and K.V.G. are supported by NASA grant NNX15AF42G and *Chandra* grant AR7-18002X, GO7-18001X, G06-17015x, and the *Chandra* ACIS Team contract SV474018 (G. Garmire & L. Townsley, Principal Investigators) issued by the *Chandra* X-ray Center under contract NAS8-03060.

Facility: *Gaia*

Software: astro (Kelvin 2014), celestial (Robotham 2016), MVN (Korkmaz et al. 2014), R (R Core Team 2018), relaimpo (Grömping et al. 2006), spatstat (Baddeley et al. 2005), TOPCAT (Taylor 2005)

REFERENCES

- Aarseth, S. J., & Hills, J. G. 1972, *A&A*, 21, 255
- Adams, F. C. 2000, *ApJ*, 542, 964, doi: [10.1086/317052](https://doi.org/10.1086/317052)
- Allison, R. J. 2012, *MNRAS*, 421, 3338, doi: [10.1111/j.1365-2966.2012.20557.x](https://doi.org/10.1111/j.1365-2966.2012.20557.x)
- Baddeley, A., Rubak, E., & Turner, R. 2015, *Spatial point patterns: methodology and applications with R* (CRC Press)
- Baddeley, A., Turner, R., et al. 2005, *Journal of statistical software*, 12, 1
- Bailer-Jones, C. A. L., Rybizki, J., Fouesneau, M., Mantelet, G., & Andrae, R. 2018, *ArXiv e-prints*. <https://arxiv.org/abs/1804.10121>
- Banerjee, S., & Kroupa, P. 2015, *MNRAS*, 447, 728, doi: [10.1093/mnras/stu2445](https://doi.org/10.1093/mnras/stu2445)
- Banerjee, S., & Kroupa, P. 2018, in *Astrophysics and Space Science Library*, Vol. 424, *The Birth of Star Clusters*, ed. S. Stahler, 143
- Bianchini, P., van de Ven, G., Norris, M. A., Schinnerer, E., & Varri, A. L. 2016, *MNRAS*, 458, 3644, doi: [10.1093/mnras/stw552](https://doi.org/10.1093/mnras/stw552)
- Bianchini, P., van der Marel, R. P., del Pino, A., et al. 2018, *ArXiv e-prints*. <https://arxiv.org/abs/1806.02580>
- Binney, J., & Tremaine, S. 2008, *Galactic Dynamics: Second Edition* (Princeton University Press)
- Blaauw, A. 1964, *ARA&A*, 2, 213, doi: [10.1146/annurev.aa.02.090164.001241](https://doi.org/10.1146/annurev.aa.02.090164.001241)
- Blitz, L., Fich, M., & Stark, A. A. 1982, *ApJS*, 49, 183, doi: [10.1086/190795](https://doi.org/10.1086/190795)
- Bonnell, I. A., Bate, M. R., & Vine, S. G. 2003, *MNRAS*, 343, 413, doi: [10.1046/j.1365-8711.2003.06687.x](https://doi.org/10.1046/j.1365-8711.2003.06687.x)
- Bravi, L., Zari, E., Sacco, G. G., et al. 2018, *ArXiv e-prints*. <https://arxiv.org/abs/1803.01908>
- Bressan, A., Marigo, P., Girardi, L., et al. 2012, *MNRAS*, 427, 127, doi: [10.1111/j.1365-2966.2012.21948.x](https://doi.org/10.1111/j.1365-2966.2012.21948.x)
- Brinkmann, N., Banerjee, S., Motwani, B., & Kroupa, P. 2017, *A&A*, 600, A49, doi: [10.1051/0004-6361/201629312](https://doi.org/10.1051/0004-6361/201629312)
- Broos, P. S., Getman, K. V., Povich, M. S., et al. 2013, *ApJS*, 209, 32, doi: [10.1088/0067-0049/209/2/32](https://doi.org/10.1088/0067-0049/209/2/32)
- Brown, A. G. A., Dekker, G., & de Zeeuw, P. T. 1997, *MNRAS*, 285, 479, doi: [10.1093/mnras/285.3.479](https://doi.org/10.1093/mnras/285.3.479)
- Cambrésy, L., Rho, J., Marshall, D. J., & Reach, W. T. 2011, *A&A*, 527, A141, doi: [10.1051/0004-6361/201015863](https://doi.org/10.1051/0004-6361/201015863)
- Caswell, J. L., & Haynes, R. F. 1987, *A&A*, 171, 261
- Clarke, C. J., Mathieu, R. D., & Reid, I. N. 2015, *Dynamics of Young Star Clusters and Associations*, 1st edn., ed. L. Eyer & C. P. Bell, *Saas-Fee Advanced Course* (Berlin: Springer)
- Cleveland, W. S. 1979, *Journal of the American statistical association*, 74, 829
- Cottaar, M., Covey, K. R., Foster, J. B., et al. 2015, *ApJ*, 807, 27, doi: [10.1088/0004-637X/807/1/27](https://doi.org/10.1088/0004-637X/807/1/27)
- Cropper, M., Katz, D., Sartoretti, P., et al. 2018, *ArXiv e-prints*. <https://arxiv.org/abs/1804.09369>
- Da Rio, N., Tan, J. C., Covey, K. R., et al. 2017, *ApJ*, 845, 105, doi: [10.3847/1538-4357/aa7a5b](https://doi.org/10.3847/1538-4357/aa7a5b)
- Dale, J. E., Ercolano, B., & Bonnell, I. A. 2015, *MNRAS*, 451, 987, doi: [10.1093/mnras/stv913](https://doi.org/10.1093/mnras/stv913)
- Damiani, F., Micela, G., & Sciortino, S. 2016, *A&A*, 596, A82, doi: [10.1051/0004-6361/201629029](https://doi.org/10.1051/0004-6361/201629029)
- Dewdney, P. E., & Roger, R. S. 1982, *ApJ*, 255, 564, doi: [10.1086/159858](https://doi.org/10.1086/159858)
- Dias, W. S., Alessi, B. S., Moitinho, A., & Lépine, J. R. D. 2002, *A&A*, 389, 871, doi: [10.1051/0004-6361:20020668](https://doi.org/10.1051/0004-6361:20020668)
- Duchêne, G., Lacour, S., Moraux, E., Goodwin, S., & Bouvier, J. 2018, *MNRAS*, doi: [10.1093/mnras/sty1180](https://doi.org/10.1093/mnras/sty1180)
- Dzib, S. A., Loinard, L., Rodríguez, L. F., et al. 2017, *ApJ*, 834, 139, doi: [10.3847/1538-4357/834/2/139](https://doi.org/10.3847/1538-4357/834/2/139)
- Elmegreen, B. G. 1983, *MNRAS*, 203, 1011, doi: [10.1093/mnras/203.4.1011](https://doi.org/10.1093/mnras/203.4.1011)
- . 2000, *ApJ*, 530, 277, doi: [10.1086/308361](https://doi.org/10.1086/308361)
- Evans, C. J., Smartt, S. J., Lee, J.-K., et al. 2005, *A&A*, 437, 467, doi: [10.1051/0004-6361:20042446](https://doi.org/10.1051/0004-6361:20042446)
- Feigelson, E. D. 2018, in *Astrophysics and Space Science Library*, Vol. 424, *The Birth of Star Clusters*, ed. S. Stahler, 119

- Feigelson, E. D., Townsley, L. K., Broos, P. S., et al. 2013, *ApJS*, 209, 26, doi: [10.1088/0067-0049/209/2/26](https://doi.org/10.1088/0067-0049/209/2/26)
- Fellhauer, M., Wilkinson, M. I., & Kroupa, P. 2009, *MNRAS*, 397, 954, doi: [10.1111/j.1365-2966.2009.15009.x](https://doi.org/10.1111/j.1365-2966.2009.15009.x)
- Fűrész, G., Hartmann, L. W., Megeath, S. T., Szentgyorgyi, A. H., & Hamden, E. T. 2008, *ApJ*, 676, 1109, doi: [10.1086/525844](https://doi.org/10.1086/525844)
- Fűrész, G., Hartmann, L. W., Szentgyorgyi, A. H., et al. 2006, *ApJ*, 648, 1090, doi: [10.1086/506140](https://doi.org/10.1086/506140)
- Fletcher, R., & Reeves, C. M. 1964, *The computer journal*, 7, 149
- Foster, J. B., Cottaar, M., Covey, K. R., et al. 2015, *ApJ*, 799, 136, doi: [10.1088/0004-637X/799/2/136](https://doi.org/10.1088/0004-637X/799/2/136)
- Fukui, Y., Ohama, A., Hanaoka, N., et al. 2014, *ApJ*, 780, 36, doi: [10.1088/0004-637X/780/1/36](https://doi.org/10.1088/0004-637X/780/1/36)
- Gaia Collaboration, Brown, A. G. A., Vallenari, A., et al. 2018a, *ArXiv e-prints*. <https://arxiv.org/abs/1804.09365>
- Gaia Collaboration, Prusti, T., de Bruijne, J. H. J., et al. 2016, *A&A*, 595, A1, doi: [10.1051/0004-6361/201629272](https://doi.org/10.1051/0004-6361/201629272)
- Gaia Collaboration, Helmi, A., van Leeuwen, F., et al. 2018b, *ArXiv e-prints*. <https://arxiv.org/abs/1804.09381>
- Galli, P. A. B., Joncour, I., & Moraux, E. 2018, *MNRAS*, 477, L50, doi: [10.1093/mnras/sly036](https://doi.org/10.1093/mnras/sly036)
- Getman, K. V., Broos, P. S., Kuhn, M. A., et al. 2017, *ApJS*, 229, 28, doi: [10.3847/1538-4365/229/2/28](https://doi.org/10.3847/1538-4365/229/2/28)
- Getman, K. V., Kuhn, M. A., Feigelson, E. D., et al. 2018a, *MNRAS*, doi: [10.1093/mnras/sty473](https://doi.org/10.1093/mnras/sty473)
- . 2018b, *MNRAS*, 477, 298, doi: [10.1093/mnras/sty473](https://doi.org/10.1093/mnras/sty473)
- Getman, K. V., Feigelson, E. D., Kuhn, M. A., et al. 2014, *ApJ*, 787, 108, doi: [10.1088/0004-637X/787/2/108](https://doi.org/10.1088/0004-637X/787/2/108)
- Goodwin, S. P., & Bastian, N. 2006, *MNRAS*, 373, 752, doi: [10.1111/j.1365-2966.2006.11078.x](https://doi.org/10.1111/j.1365-2966.2006.11078.x)
- Gouliermis, D. A. 2018, *Publications of the Astronomical Society of the Pacific*, 130, 072001
- Grömping, U., et al. 2006, *Journal of statistical software*, 17, 1
- Henney, W. J., & Arthur, S. J. 1998, *AJ*, 116, 322, doi: [10.1086/300433](https://doi.org/10.1086/300433)
- Henze, N., & Zirkler, B. 1990, *Communications in Statistics-Theory and Methods*, 19, 3595
- Hillenbrand, L. A., & Hartmann, L. W. 1998, *ApJ*, 492, 540, doi: [10.1086/305076](https://doi.org/10.1086/305076)
- Hills, J. G. 1980, *ApJ*, 235, 986, doi: [10.1086/157703](https://doi.org/10.1086/157703)
- Hirota, T., Bushimata, T., Choi, Y. K., et al. 2008, *PASJ*, 60, 37, doi: [10.1093/pasj/60.1.37](https://doi.org/10.1093/pasj/60.1.37)
- Hollander, M., & Wolfe, D. 1973, *Nonparametric statistical methods*, Wiley Series in Probability and Statistics - Applied Probability and Statistics Section (Wiley). <https://books.google.com/books?id=ajxMAAAAMAAJ>
- Ibáñez-Mejía, J. C., Mac Low, M.-M., Klessen, R. S., & Baczynski, C. 2017, *ApJ*, 850, 62, doi: [10.3847/1538-4357/aa93fe](https://doi.org/10.3847/1538-4357/aa93fe)
- Jones, B. F., & Walker, M. F. 1988, *AJ*, 95, 1755, doi: [10.1086/114773](https://doi.org/10.1086/114773)
- Kamann, S., Husser, T. O., Dreizler, S., et al. 2018, *MNRAS*, 473, 5591, doi: [10.1093/mnras/stx2719](https://doi.org/10.1093/mnras/stx2719)
- Kelvin, L. 2014, *astro: Astronomy Functions, Tools and Routines*, 1.2, CRAN. <https://CRAN.R-project.org/package=astro>
- Kharchenko, N. V., Piskunov, A. E., Röser, S., Schilbach, E., & Scholz, R.-D. 2005, *A&A*, 438, 1163, doi: [10.1051/0004-6361:20042523](https://doi.org/10.1051/0004-6361:20042523)
- Kim, B. G., Kawamura, A., Yonekura, Y., & Fukui, Y. 2004, *PASJ*, 56, 313, doi: [10.1093/pasj/56.2.313](https://doi.org/10.1093/pasj/56.2.313)
- King, I. R. 1966, *AJ*, 71, 64, doi: [10.1086/109857](https://doi.org/10.1086/109857)
- Korkmaz, S., Goksuluk, D., & Zararsiz, G. 2014, *The R Journal*, 6, 151
- Kounkel, M., Hartmann, L., Tobin, J. J., et al. 2016a, *ApJ*, 821, 8, doi: [10.3847/0004-637X/821/1/8](https://doi.org/10.3847/0004-637X/821/1/8)
- Kounkel, M., Hartmann, L., Loinard, L., et al. 2016b, *ArXiv e-prints*. <https://arxiv.org/abs/1609.04041>
- Kounkel, M., Covey, K., Suarez, G., et al. 2018, *ArXiv e-prints*. <https://arxiv.org/abs/1805.04649>
- Kroupa, P., Aarseth, S., & Hurley, J. 2001, *MNRAS*, 321, 699, doi: [10.1046/j.1365-8711.2001.04050.x](https://doi.org/10.1046/j.1365-8711.2001.04050.x)
- Kruijssen, J. M. D. 2012, *MNRAS*, 426, 3008, doi: [10.1111/j.1365-2966.2012.21923.x](https://doi.org/10.1111/j.1365-2966.2012.21923.x)
- Krumholz, M. R., & McKee, C. F. 2005, *ApJ*, 630, 250, doi: [10.1086/431734](https://doi.org/10.1086/431734)
- Kuhn, M. A., & Feigelson, E. D. 2017, *ArXiv e-prints*. <https://arxiv.org/abs/1711.11101>
- Kuhn, M. A., Feigelson, E. D., Getman, K. V., et al. 2015a, *ApJ*, 812, 131, doi: [10.1088/0004-637X/812/2/131](https://doi.org/10.1088/0004-637X/812/2/131)
- Kuhn, M. A., Getman, K. V., & Feigelson, E. D. 2015b, *ApJ*, 802, 60, doi: [10.1088/0004-637X/802/1/60](https://doi.org/10.1088/0004-637X/802/1/60)
- Kuhn, M. A., Getman, K. V., Feigelson, E. D., et al. 2017a, *AJ*, 154, 214, doi: [10.3847/1538-3881/aa9177](https://doi.org/10.3847/1538-3881/aa9177)
- Kuhn, M. A., Medina, N., Getman, K. V., et al. 2017b, *AJ*, 154, 87, doi: [10.3847/1538-3881/aa76e8](https://doi.org/10.3847/1538-3881/aa76e8)
- Kuhn, M. A., Feigelson, E. D., Getman, K. V., et al. 2014, *ApJ*, 787, 107, doi: [10.1088/0004-637X/787/2/107](https://doi.org/10.1088/0004-637X/787/2/107)
- Kuznetsova, A., Hartmann, L., & Ballesteros-Paredes, J. 2015a, *ApJ*, 815, 27, doi: [10.1088/0004-637X/815/1/27](https://doi.org/10.1088/0004-637X/815/1/27)
- . 2015b, *ApJ*, 815, 27, doi: [10.1088/0004-637X/815/1/27](https://doi.org/10.1088/0004-637X/815/1/27)
- Lada, C. J., & Lada, E. A. 2003, *ARA&A*, 41, 57, doi: [10.1146/annurev.astro.41.011802.094844](https://doi.org/10.1146/annurev.astro.41.011802.094844)
- Lada, E. A., & Lada, C. J. 1995, *AJ*, 109, 1682, doi: [10.1086/117396](https://doi.org/10.1086/117396)

- Larson, R. B. 1981, *MNRAS*, 194, 809, doi: [10.1093/mnras/194.4.809](https://doi.org/10.1093/mnras/194.4.809)
- Lee, Y.-N., & Hennebelle, P. 2016, *A&A*, 591, A30, doi: [10.1051/0004-6361/201527981](https://doi.org/10.1051/0004-6361/201527981)
- Lindegren, L., Lammers, U., Hobbs, D., et al. 2012, *A&A*, 538, A78, doi: [10.1051/0004-6361/201117905](https://doi.org/10.1051/0004-6361/201117905)
- Lindegren, L., Lammers, U., Bastian, U., et al. 2016, *ArXiv e-prints*. <https://arxiv.org/abs/1609.04303>
- Lindegren, L., Hernandez, J., Bombrun, A., et al. 2018, *ArXiv e-prints*. <https://arxiv.org/abs/1804.09366>
- Liu, T., Janes, K. A., & Bania, T. M. 1989, *AJ*, 98, 626, doi: [10.1086/115162](https://doi.org/10.1086/115162)
- . 1991, *AJ*, 102, 1103, doi: [10.1086/115936](https://doi.org/10.1086/115936)
- Luhman, K. L., Esplin, T. L., & Loutrel, N. P. 2016, *ApJ*, 827, 52, doi: [10.3847/0004-637X/827/1/52](https://doi.org/10.3847/0004-637X/827/1/52)
- Mac Low, M.-M., & Klessen, R. S. 2004, *Reviews of Modern Physics*, 76, 125, doi: [10.1103/RevModPhys.76.125](https://doi.org/10.1103/RevModPhys.76.125)
- Mapelli, M. 2017, *MNRAS*, 467, 3255, doi: [10.1093/mnras/stx304](https://doi.org/10.1093/mnras/stx304)
- Marks, M., & Kroupa, P. 2012, *A&A*, 543, A8, doi: [10.1051/0004-6361/201118231](https://doi.org/10.1051/0004-6361/201118231)
- Maschberger, T. 2013, *MNRAS*, 429, 1725, doi: [10.1093/mnras/sts479](https://doi.org/10.1093/mnras/sts479)
- Maschberger, T., Clarke, C. J., Bonnell, I. A., & Kroupa, P. 2010, *MNRAS*, 404, 1061, doi: [10.1111/j.1365-2966.2010.16346.x](https://doi.org/10.1111/j.1365-2966.2010.16346.x)
- Mathieu, R. D. 1983, *ApJL*, 267, L97, doi: [10.1086/184011](https://doi.org/10.1086/184011)
- McLachlan, G., & Peel, D. 2000, *Finite mixture models* (John Wiley & Sons)
- Megeath, S. T., Gutermuth, R., Muzerolle, J., et al. 2016, *AJ*, 151, 5, doi: [10.3847/0004-6256/151/1/5](https://doi.org/10.3847/0004-6256/151/1/5)
- Menten, K. M., Reid, M. J., Forbrich, J., & Brunthaler, A. 2007, *A&A*, 474, 515, doi: [10.1051/0004-6361:20078247](https://doi.org/10.1051/0004-6361:20078247)
- Moraux, E. 2016, in *EAS Publications Series*, Vol. 80, *EAS Publications Series*, ed. E. Moraux, Y. Lebreton, & C. Charbonnel, 73–114
- Muench, A., Getman, K., Hillenbrand, L., & Preibisch, T. 2008, *Star Formation in the Orion Nebula I: Stellar Content*, ed. B. Reipurth, 483
- Muraveva, T., Delgado, H. E., Clementini, G., Sarro, L. M., & Garofalo, A. 2018, *ArXiv e-prints*. <https://arxiv.org/abs/1805.08742>
- Naylor, T., Broos, P. S., & Feigelson, E. D. 2013, *ApJS*, 209, 30, doi: [10.1088/0067-0049/209/2/30](https://doi.org/10.1088/0067-0049/209/2/30)
- O'dell, C. R. 2001, *ARA&A*, 39, 99, doi: [10.1146/annurev.astro.39.1.99](https://doi.org/10.1146/annurev.astro.39.1.99)
- Padoan, P., & Nordlund, Å. 2002, *ApJ*, 576, 870, doi: [10.1086/341790](https://doi.org/10.1086/341790)
- Parker, R. J., Goodwin, S. P., Wright, N. J., Meyer, M. R., & Quanz, S. P. 2016, *MNRAS*, 459, L119, doi: [10.1093/mnrasl/slw061](https://doi.org/10.1093/mnrasl/slw061)
- Parker, R. J., & Wright, N. J. 2016, *MNRAS*, 457, 3430, doi: [10.1093/mnras/stw087](https://doi.org/10.1093/mnras/stw087)
- Parker, R. J., Wright, N. J., Goodwin, S. P., & Meyer, M. R. 2014, *MNRAS*, 438, 620, doi: [10.1093/mnras/stt2231](https://doi.org/10.1093/mnras/stt2231)
- Pecaut, M. J., & Mamajek, E. E. 2016, *MNRAS*, 461, 794, doi: [10.1093/mnras/stw1300](https://doi.org/10.1093/mnras/stw1300)
- Pelupessy, F. I., & Portegies Zwart, S. 2012, *MNRAS*, 420, 1503, doi: [10.1111/j.1365-2966.2011.20137.x](https://doi.org/10.1111/j.1365-2966.2011.20137.x)
- Pfalzner, S. 2009, *A&A*, 498, L37, doi: [10.1051/0004-6361/200912056](https://doi.org/10.1051/0004-6361/200912056)
- . 2011, *A&A*, 536, A90, doi: [10.1051/0004-6361/201117777](https://doi.org/10.1051/0004-6361/201117777)
- Pfalzner, S., Parmentier, G., Steinhausen, M., Vincke, K., & Menten, K. 2014, *ApJ*, 794, 147, doi: [10.1088/0004-637X/794/2/147](https://doi.org/10.1088/0004-637X/794/2/147)
- Povich, M. S., Kuhn, M. A., Getman, K. V., et al. 2013, *ApJS*, 209, 31, doi: [10.1088/0067-0049/209/2/31](https://doi.org/10.1088/0067-0049/209/2/31)
- Pozzo, M., Naylor, T., Jeffries, R. D., & Drew, J. E. 2003, *MNRAS*, 341, 805, doi: [10.1046/j.1365-8711.2003.06447.x](https://doi.org/10.1046/j.1365-8711.2003.06447.x)
- Preibisch, T., & Mamajek, E. 2008, *The Nearest OB Association: Scorpius-Centaurus (Sco OB2)*, ed. B. Reipurth, 235
- Proszkow, E.-M., Adams, F. C., Hartmann, L. W., & Tobin, J. J. 2009, *ApJ*, 697, 1020, doi: [10.1088/0004-637X/697/2/1020](https://doi.org/10.1088/0004-637X/697/2/1020)
- R Core Team. 2018, *R: A Language and Environment for Statistical Computing*, R Foundation for Statistical Computing, Vienna, Austria
- Reino, S., de Bruijne, J., Zari, E., d'Antona, F., & Ventura, P. 2018, *MNRAS*, 477, 3197, doi: [10.1093/mnras/sty793](https://doi.org/10.1093/mnras/sty793)
- Richert, A. J. W., Getman, K. V., Feigelson, E. D., et al. 2018, *MNRAS*, 477, 5191, doi: [10.1093/mnras/sty949](https://doi.org/10.1093/mnras/sty949)
- Rieke, G. H., & Lebofsky, M. J. 1985, *ApJ*, 288, 618, doi: [10.1086/162827](https://doi.org/10.1086/162827)
- Rivilla, V. M., Martín-Pintado, J., Jiménez-Serra, I., & Rodríguez-Franco, A. 2013, *A&A*, 554, A48, doi: [10.1051/0004-6361/201117487](https://doi.org/10.1051/0004-6361/201117487)
- Robotham, A. S. G. 2016, *Celestial: Common astronomical conversion routines and functions*, *Astrophysics Source Code Library*. <http://ascl.net/1602.011>
- Schwarz, G., et al. 1978, *The annals of statistics*, 6, 461
- Sills, A., Rieder, S., Scora, J., McCloskey, J., & Jaffa, S. 2018, *MNRAS*, doi: [10.1093/mnras/sty681](https://doi.org/10.1093/mnras/sty681)
- Spera, M., Mapelli, M., & Jeffries, R. D. 2016, *MNRAS*, 460, 317, doi: [10.1093/mnras/stw998](https://doi.org/10.1093/mnras/stw998)
- Spitzer, Jr., L. 1969, *ApJL*, 158, L139, doi: [10.1086/180451](https://doi.org/10.1086/180451)

- Stassun, K. G., & Torres, G. 2018, ArXiv e-prints.
<https://arxiv.org/abs/1805.03526>
- Taylor, M. B. 2005, in *Astronomical Society of the Pacific Conference Series*, Vol. 347, *Astronomical Data Analysis Software and Systems XIV*, ed. P. Shopbell, M. Britton, & R. Ebert, 29
- Tobin, J. J., Hartmann, L., Furesz, G., Mateo, M., & Megeath, S. T. 2009, *ApJ*, 697, 1103,
doi: [10.1088/0004-637X/697/2/1103](https://doi.org/10.1088/0004-637X/697/2/1103)
- Tutukov, A. V. 1978, *A&A*, 70, 57
- van Leeuwen, F. 2009, *A&A*, 497, 209,
doi: [10.1051/0004-6361/200811382](https://doi.org/10.1051/0004-6361/200811382)
- Vázquez-Semadeni, E., González-Samaniego, A., & Colín, P. 2017, *MNRAS*, 467, 1313, doi: [10.1093/mnras/stw3229](https://doi.org/10.1093/mnras/stw3229)
- Walker, M. G., Mateo, M., Olszewski, E. W., et al. 2006, *AJ*, 131, 2114, doi: [10.1086/500193](https://doi.org/10.1086/500193)
- Ward, J. L., & Kruijssen, J. M. D. 2018, *MNRAS*, 475, 5659, doi: [10.1093/mnras/sty117](https://doi.org/10.1093/mnras/sty117)
- Webb, J. J., & Vesperini, E. 2017, *MNRAS*, 464, 1977,
doi: [10.1093/mnras/stw2513](https://doi.org/10.1093/mnras/stw2513)
- Wright, N. J., Bouy, H., Drew, J. E., et al. 2016, *MNRAS*, 460, 2593, doi: [10.1093/mnras/stw1148](https://doi.org/10.1093/mnras/stw1148)
- Wright, N. J., & Mamajek, E. E. 2018, *MNRAS*, 476, 381,
doi: [10.1093/mnras/sty207](https://doi.org/10.1093/mnras/sty207)

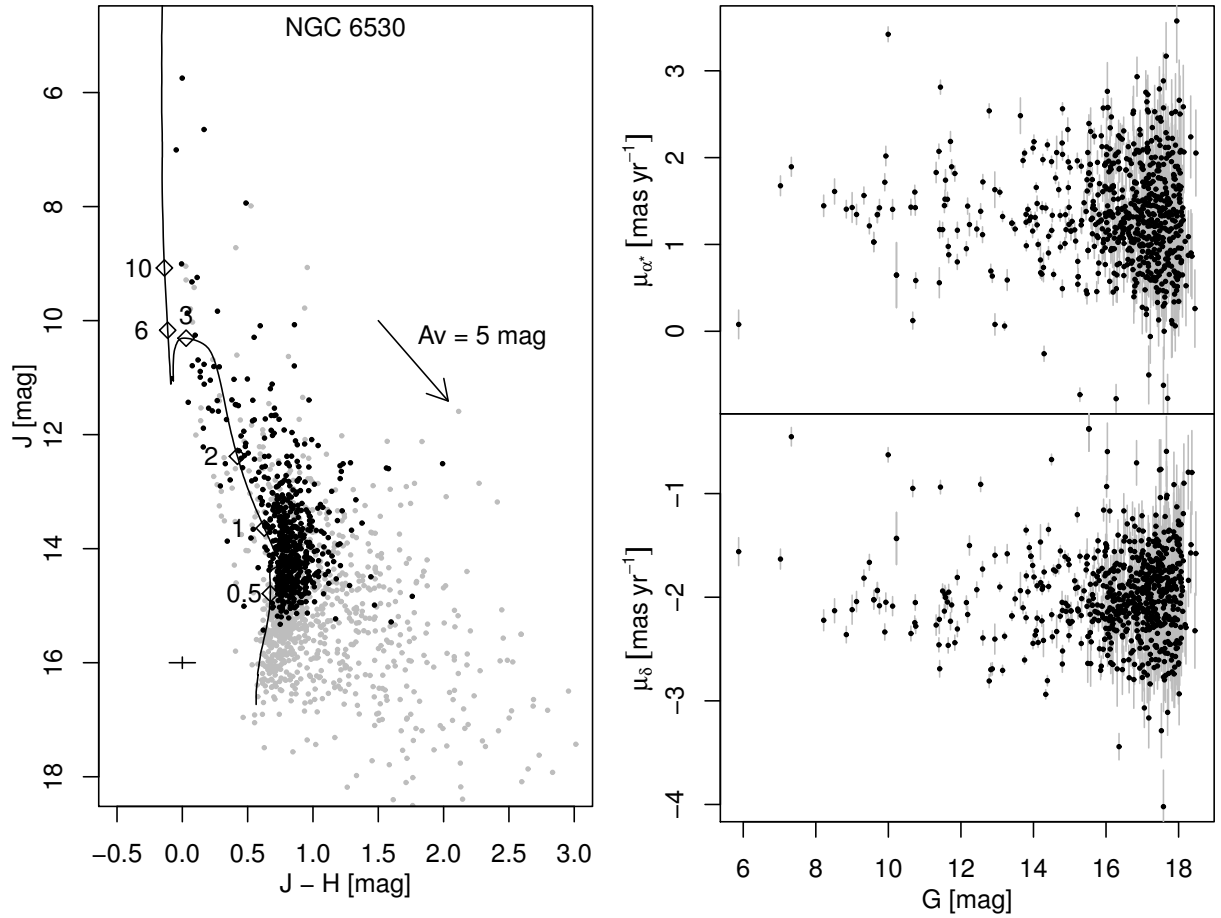


Figure 1. Left: J vs. $J-H$ color-magnitude diagram for sources in NGC 6530. *Gaia* sources used in the analysis are shown in black, while other MYStIX probable cluster members are shown in gray. Only sources with uncertainties in J and $J - H$ less than 0.1 mag are plotted. A reddening vector (Rieke & Lebofsky 1985), a 2 Myr isochrone (Bressan et al. 2012) with several masses indicated, and a cross showing maximum allowed 1σ uncertainties are shown for guidance. Right: Proper motion measurements and uncertainties vs. G -band magnitude for YSOs in NGC 6530. Only sources included in the study are plotted. Plots for other clusters are included in an online figure set.

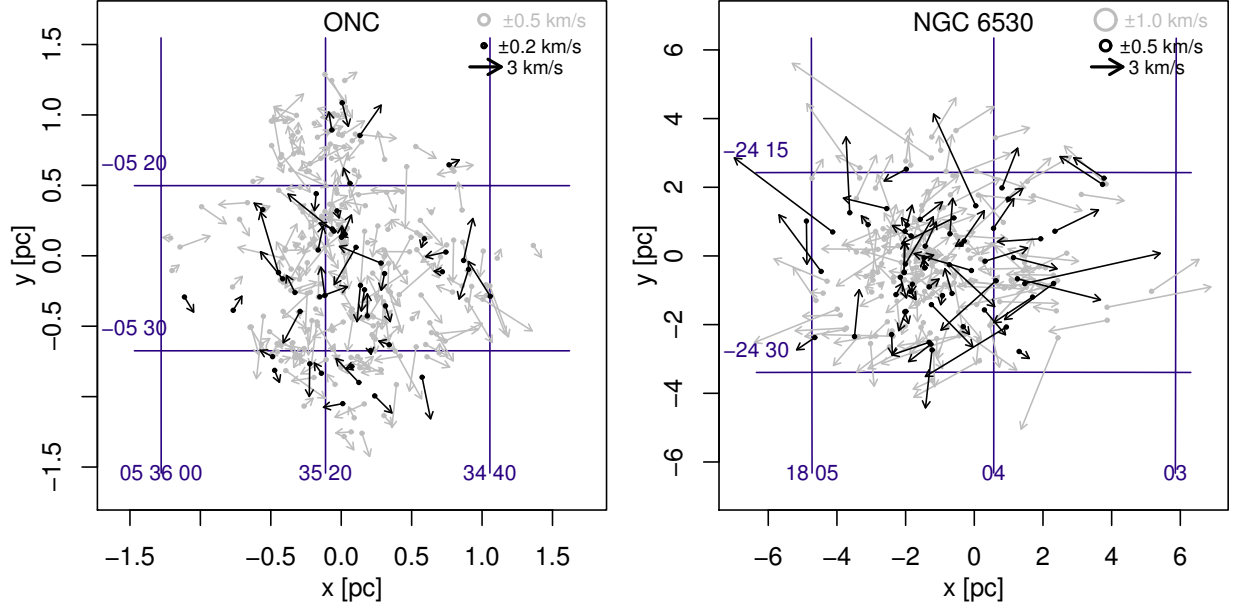


Figure 2. Maps of velocity vectors (magnitude and direction) for the best quality *Gaia* data in the ONC (left) and NGC 6530 (right). The quality of the velocity measurements are indicated by the arrow color (black for most precise and gray for less precise), with maximum allowed uncertainties for each group shown by the circles in the legend. Plots for other clusters are included in an online figure set.

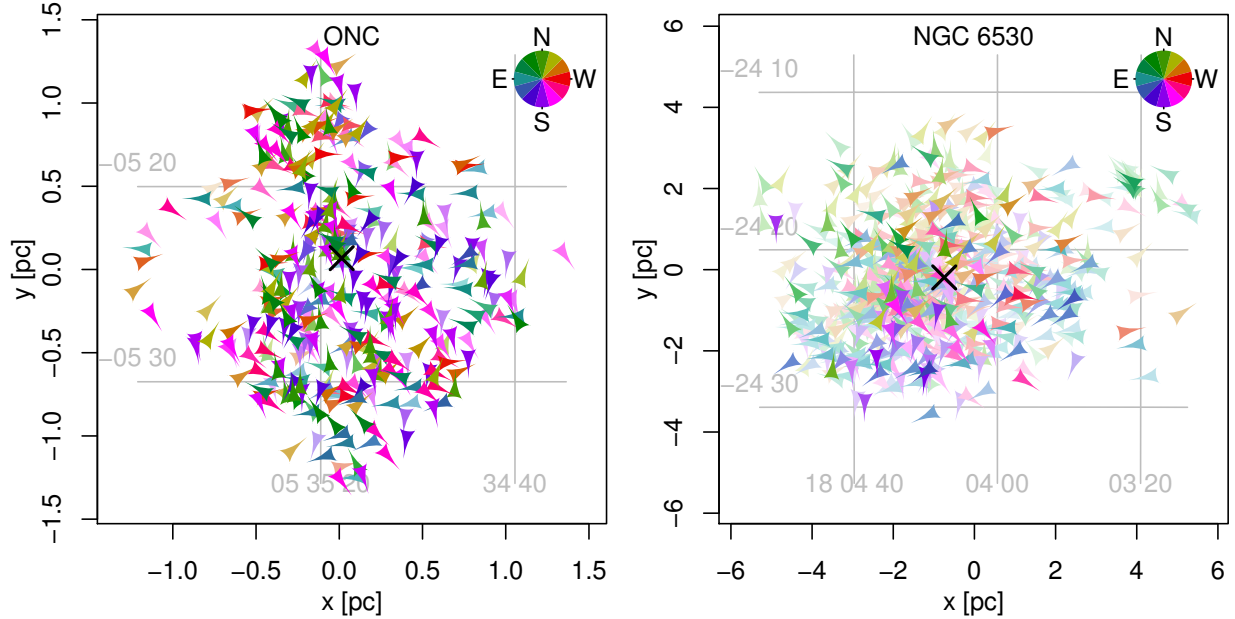


Figure 3. Direction of motion of individual stars in the rest frame of the cluster. Diagrams are shown for the ONC (left) and NGC 6530 (right). The orientations of the arrows and their hues indicate their direction, while saturation indicates weighting based on statistical uncertainty. In the ONC stars with different velocities are mixed together, while, in NGC 6530, many stars have directions of motions away from the cluster center (as indicated by the outward pointing arrows and color segregation by azimuth). Plots for other clusters are included in an online figure set.

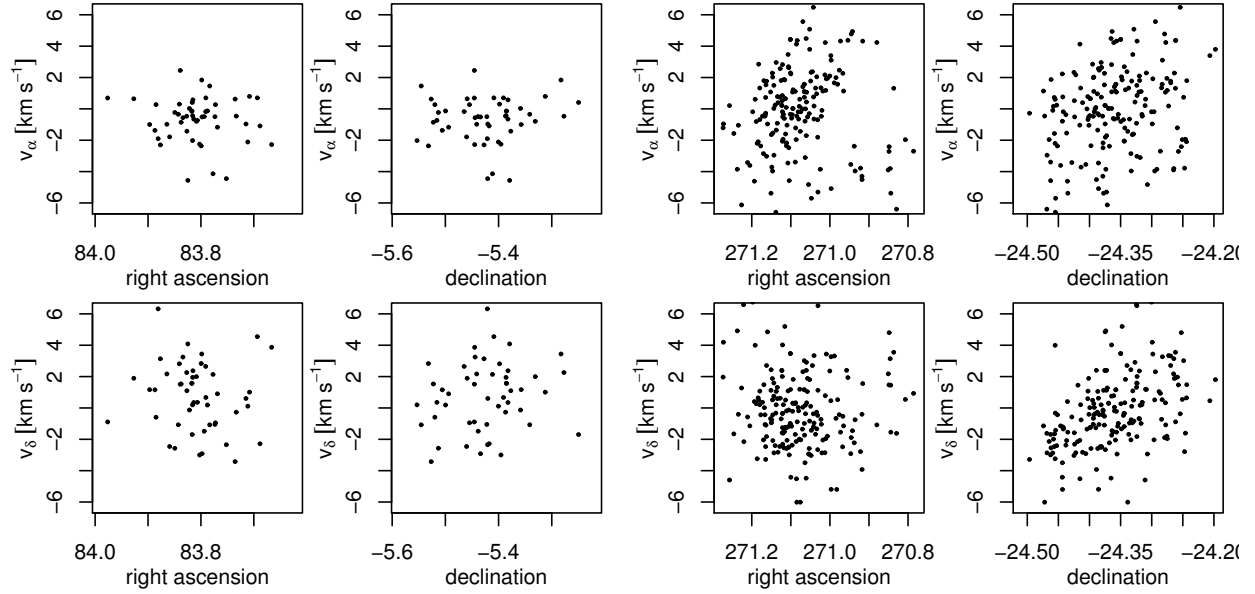


Figure 4. Dispersions of stars in position (x -axis) and velocity (y -axis) for the ONC (left) and NGC 6530 (right) are shown. For each cluster, the four panels show all combinations of right ascension, declination, v_α , and v_δ . The y -axes for all panels shows the same velocity range to facilitate comparison of velocity dispersions. Cluster expansion may show up as a correlation between right ascension and v_α or declination and v_δ . Only stars with no astrometric excess noise are included to reduce the presence of velocity outliers. Plots for other clusters are included in an online figure set.

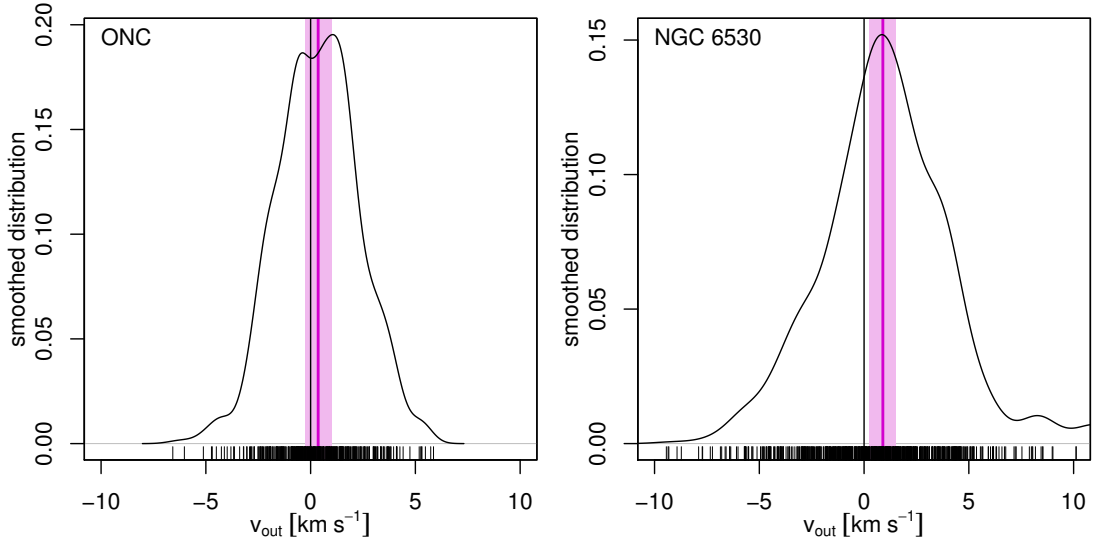


Figure 5. Distributions of v_{out} shown as KDE plots for stars in the ONC (left) and NGC 6530 (right). The black lines indicates $v_{\text{out}} = 0 \text{ km s}^{-1}$, the solid magenta line indicates the median of the distribution, and the shaded magenta region indicates the 3σ uncertainty on the median. Medians greater than 0 indicate bulk expansion while medians less than zero indicate bulk contraction. Plots for other clusters are included in an online figure set.

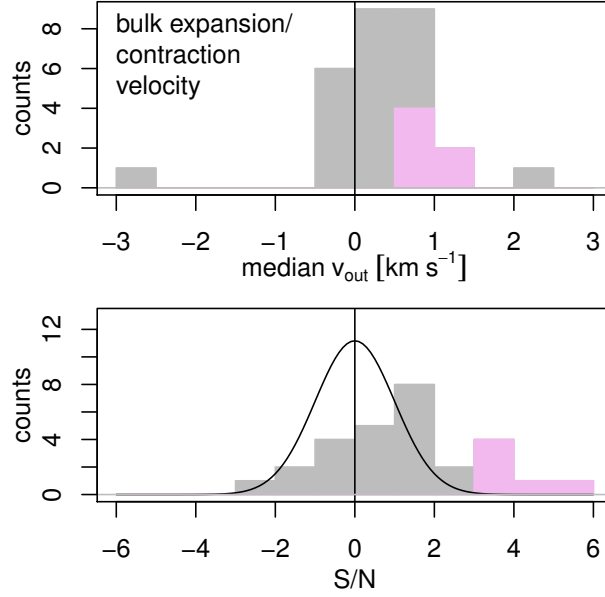


Figure 6. Histograms of expansion velocities (top) and signal-to-noise of expansion velocities (bottom) for the clusters in our sample. Clusters significant at the $>3\sigma$ level are marked in magenta. The Gaussian curve in the bottom plot shows the distribution that would be expected under the null-hypothesis that all measurements of expansion and contraction were products of measurement uncertainty.

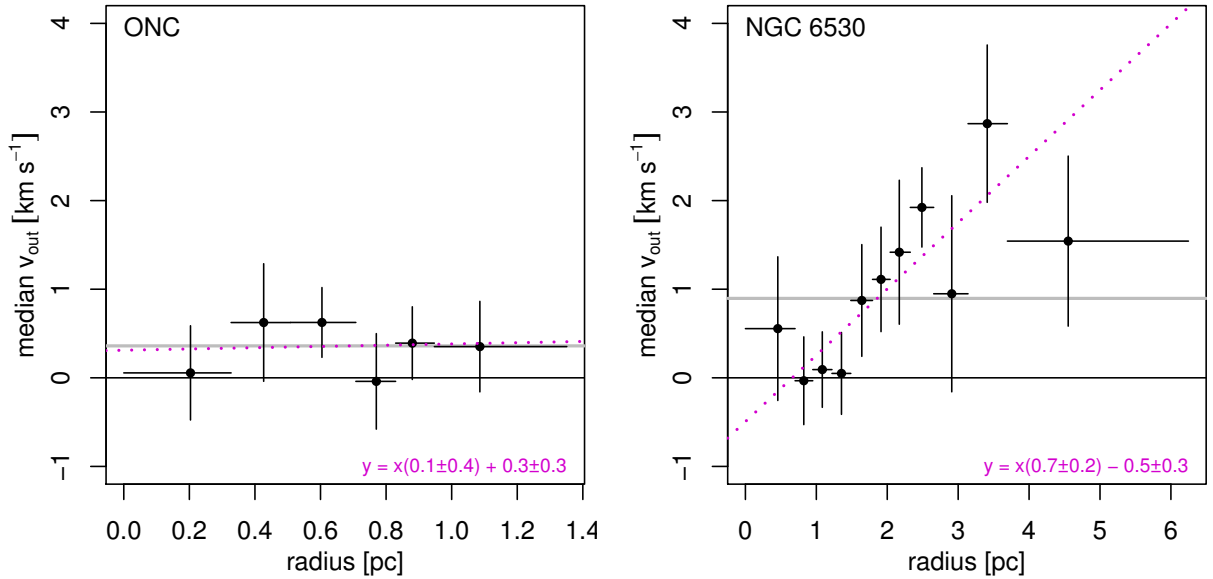


Figure 7. Expansion velocity as a function of distance from the cluster center. Stars are binned by radial distance in groups of 60. In each panel, the black line indicates the division between contraction and expansion, the gray line is the median value for the cluster as a whole, the points are the binned data, and the magenta line is a linear regression to the data. The equation of the regression line is included on the plot. Plots for other clusters are included in an online figure set.

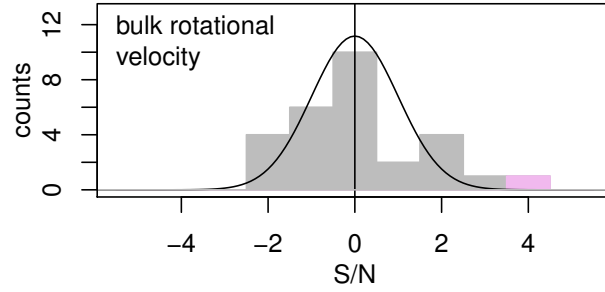


Figure 8. Histogram of signal-to-noise in rotational velocity (median v_{az} divided its uncertainty). The observed distribution is compared to the expected Gaussian distribution (black curve) for the null hypothesis that there is no rotation and non-zero values are effects of measurement uncertainty. Tr 15, significant at 4σ , is highlighted in magenta.

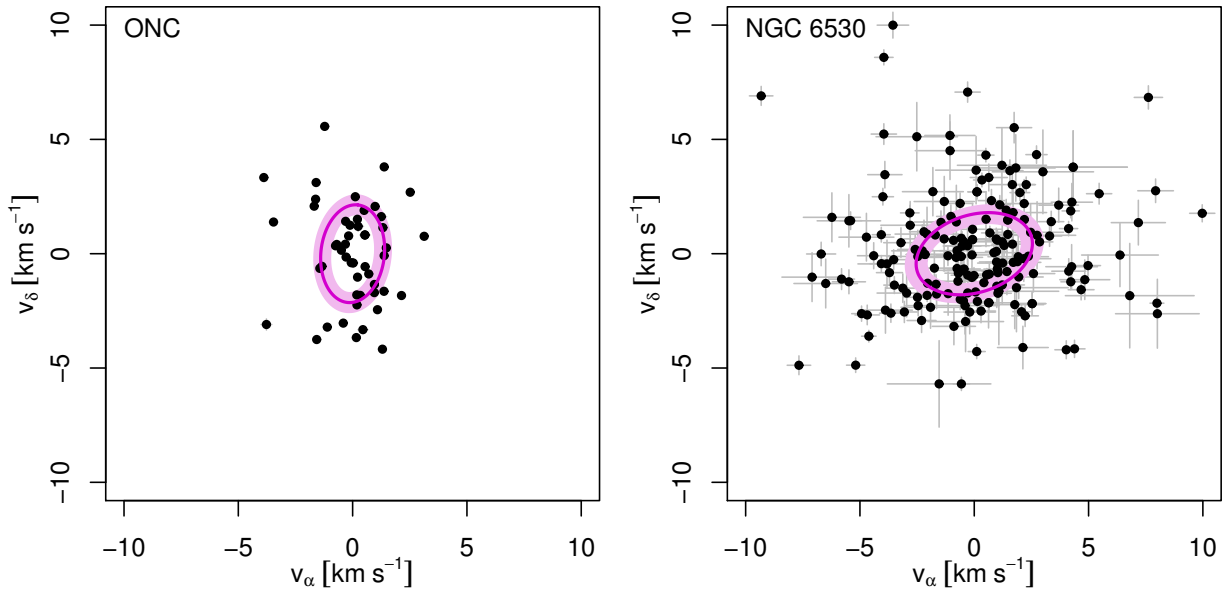


Figure 9. Velocity distributions for the ONC (left) and NGC 6530 (right). The magenta ellipses shows velocity dispersion from the best-fit bivariate normal distribution – the ellipse is the iso-density contour for this normal distribution at the 1σ level. The shaded regions shows uncertainty resulting from 2 times the standard error on the velocity dispersions. Only sources with no astrometric excess noise are used. Plots for other clusters are included in an online figure set.

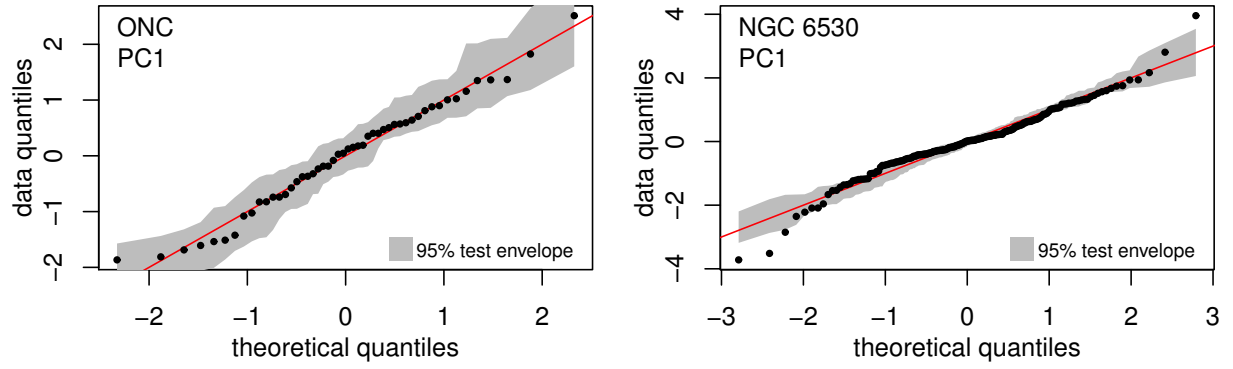


Figure 10. Q–Q plot to evaluate the Gaussianity of stellar velocity distributions. The plots show theoretical quantiles versus data quantiles, assuming that the data is fit by a normal distribution. Lower values on the left and higher values on the right show an excess number of outliers with higher than expected velocities. The red line shows the expected value for a normal distribution, and the gray shaded region shows a 95% test envelope. Only sources with no astrometric excess noise are used. Plots of v_{pc1} and v_{pc2} for other clusters are included in an online figure set.

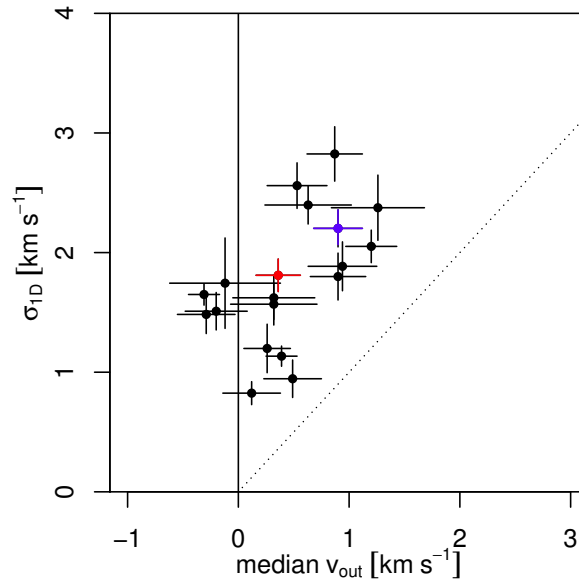


Figure 11. One-dimensional velocity dispersion versus expansion velocity. The solid line indicates the division between contracting and expanding clusters, and the dashed line indicates where both quantities are equal. The data points for the ONC (red) and NGC 6530 (blue) are marked.

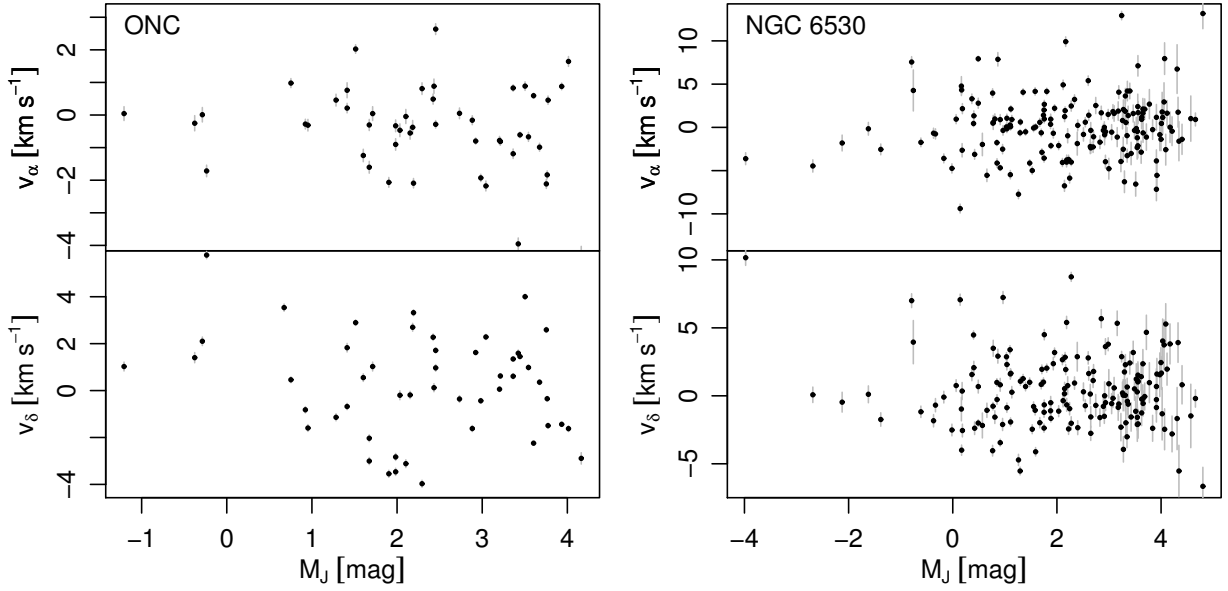


Figure 12. Velocity components v_α and v_δ versus J -band absolute magnitude. Statistical 1σ uncertainties on velocities are shown by the gray error bars. Only sources with no astrometric excess noise are used.

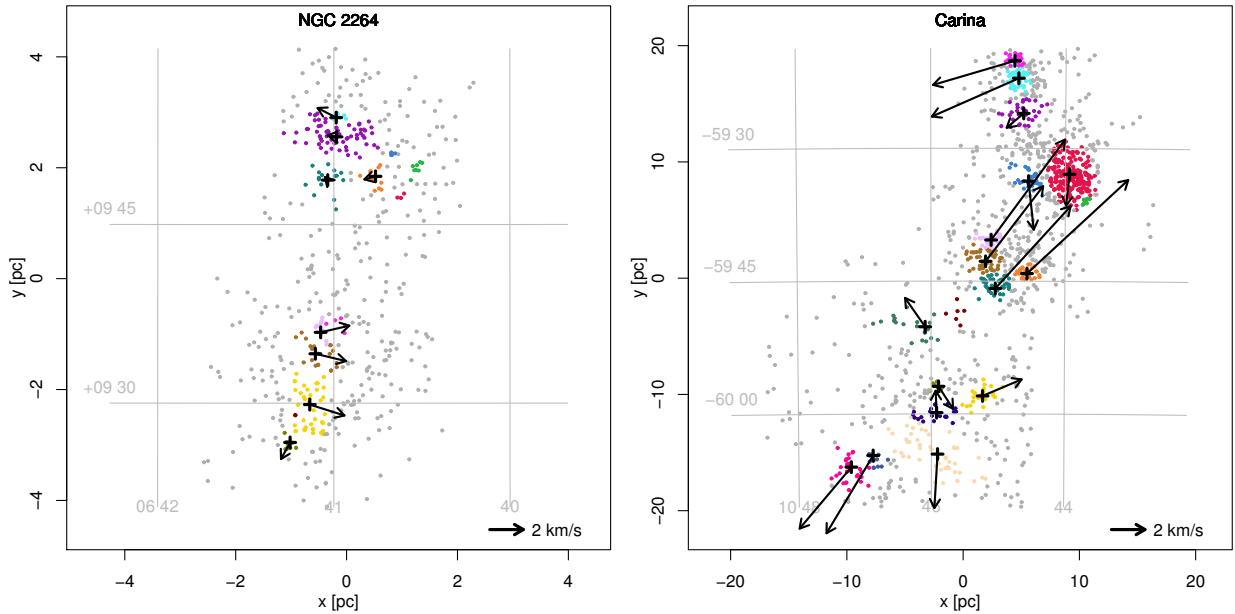


Figure 13. Kinematics of subclusters in NGC 2264 (left) and the Carina OB1 association (right). Stars included in the study are marked with a color symbol indicating the subcluster to which they were assigned in Kuhn et al. (2014). The crosses mark subcluster centers and the vectors indicate velocities of the subclusters, as indicated by the velocity scale. Subcluster velocities in Carina tend to be much larger than in the smaller, nearby NGC 2264 region. In both NGC 2264 and Carina, nearby groups of stars tend to move in similar directions, but there is no overall sign of subcluster mergers. Plots for other regions are included in an online figure set.

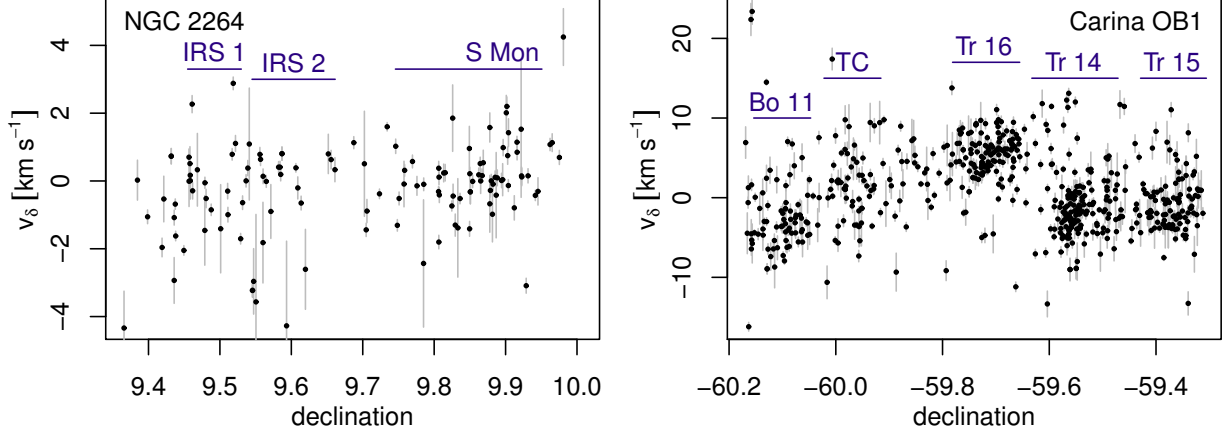


Figure 14. Velocity v_δ vs. declination for stars in NGC 2264 (left) and the Carina OB1 association (right). The declination range of several constituent clusters are marked, including S Mon, IRS 1 and IRS 2 in NGC 2264, and Tr 14, 15, 16, the Treasure Chest (TC) and Bochum 11 (Bo 11) in Carina. The plot reveals different mean velocities of different clusters as well as cluster expansion within some individual clusters. Note that the velocity range for NGC 2264 is much smaller than for Carina. Only sources with no astrometric excess noise are used.

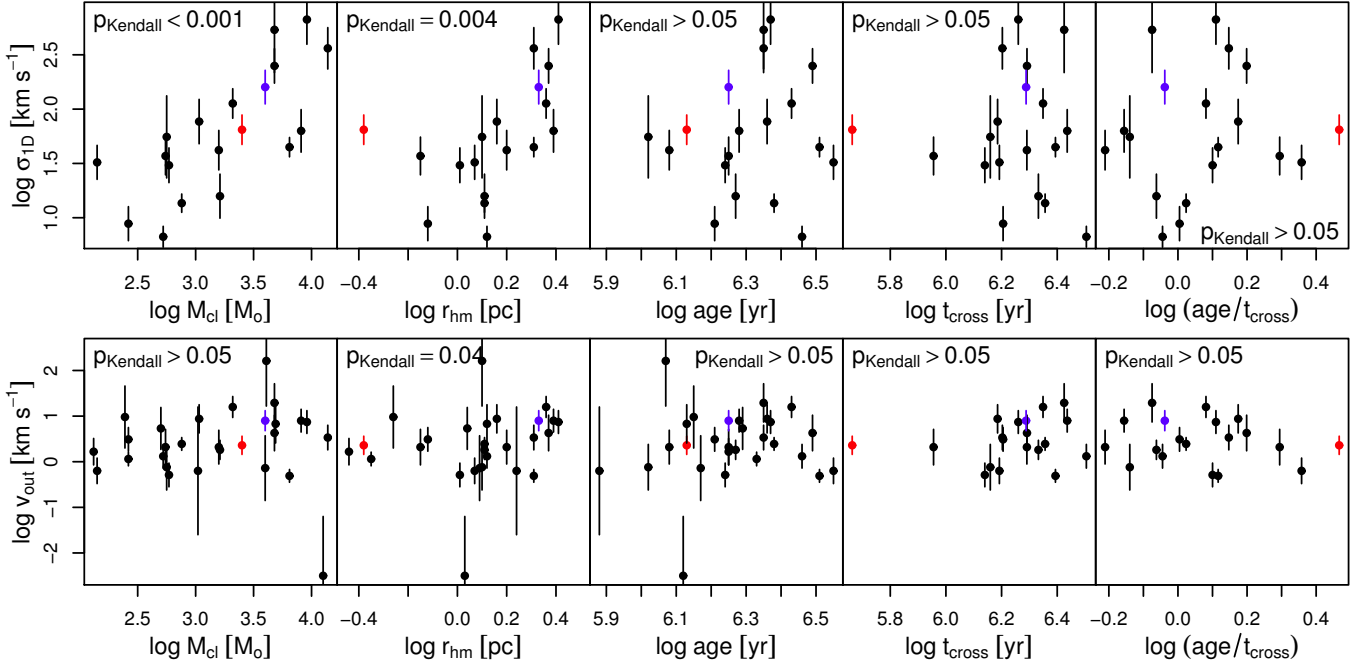


Figure 15. Scatter plots showing relationships between cluster kinematics and other physical cluster properties. Kinematics quantities include velocity dispersion (σ_{1D}) and expansion velocity (median v_{out}) from Tables 2 and 3. The other physical properties include cluster mass (M_{cl}), cluster size (r_{hm}), and cluster age, cluster crossing time (t_{cross}), and the ratio of age to crossing time. Statistical significance of correlation is assessed using the Kendall rank correlation test (Hollander & Wolfe 1973), and the p -values are shown on the plot. Positive correlations exist between velocity dispersion, cluster mass, and cluster size, but no statistically significant correlations can be found for other properties. The data points for the ONC (red) and NGC 6530 (blue) are marked.

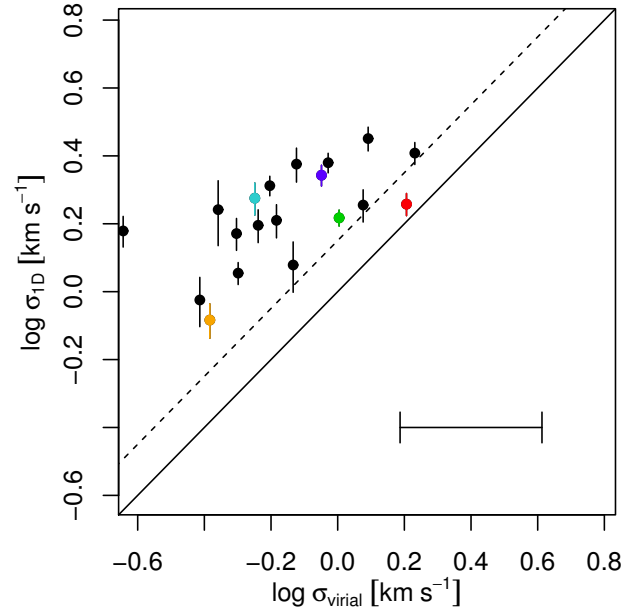


Figure 16. Virial velocity dispersion calculated using observed M_{cl} and r_{hm} versus observed velocity dispersion assuming a Plummer Sphere cluster model. Three non-expanding clusters are highlighted: the ONC (red), NGC 6231 (green), and NGC 2362 (orange). Two expanding clusters are highlighted: NGC 6530 (blue), and Cep B (cyan). The solid line shows the expected relationship for a cluster in virial equilibrium, while the dashed line shows the limit for a bound cluster. The large error bar shows how a factor of 2 uncertainty on cluster mass and cluster radius would affect σ_{virial} .

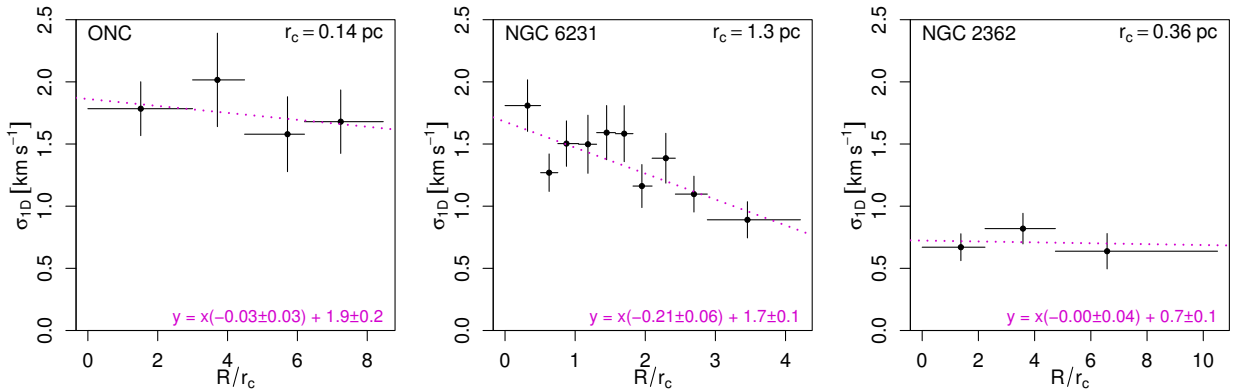


Figure 17. Velocity dispersion as a function of distance from the cluster center, scaled by the cluster core radius. In each panel, the points show the velocity dispersion in each radial bin, the error bars show 1σ uncertainties, and the dotted magenta line shows a linear regression fit to the data. The equation of the regression line for the relationship between σ_{1D} and R/r_c is included on the plot.

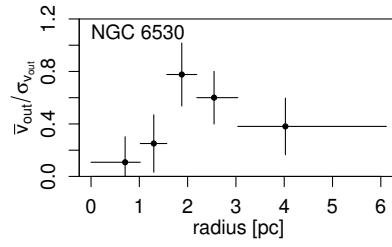


Figure 18. Ratio of expansion velocity to dispersion in v_{out} as a function of radius. Larger values indicate that velocity vectors are mostly directed outward, while smaller values indicate significant fractions of stars moving both outward and inward.

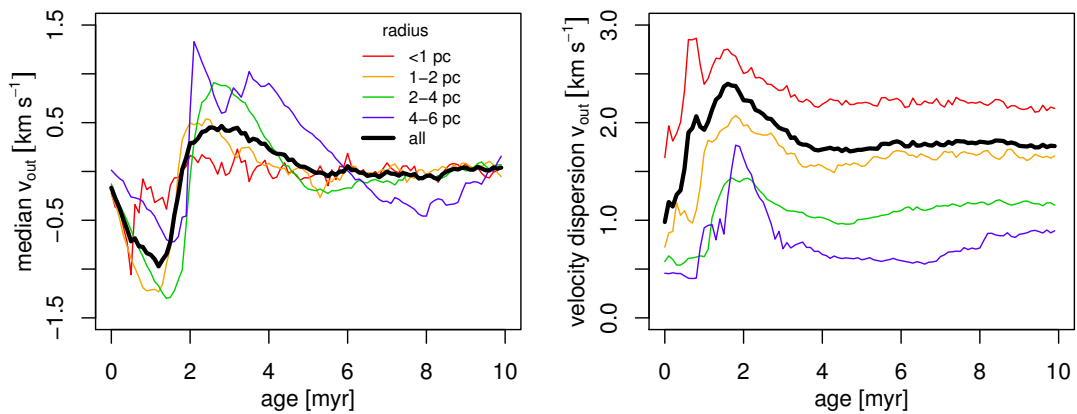


Figure 19. Characteristics of the velocity distribution for the stars in the [Sills et al. \(2018\)](#) simulation as a function of time. The left panel shows median v_{out} while the right panel shows the standard deviation of v_{out} . These statistics are calculated for stars in various radial bins as indicated by the legend. During the simulation, stars stream into the center of the cluster, yielding bulk inward velocities, before rebounding with a bulk outward velocity, and settling into a “quasi-static” state.

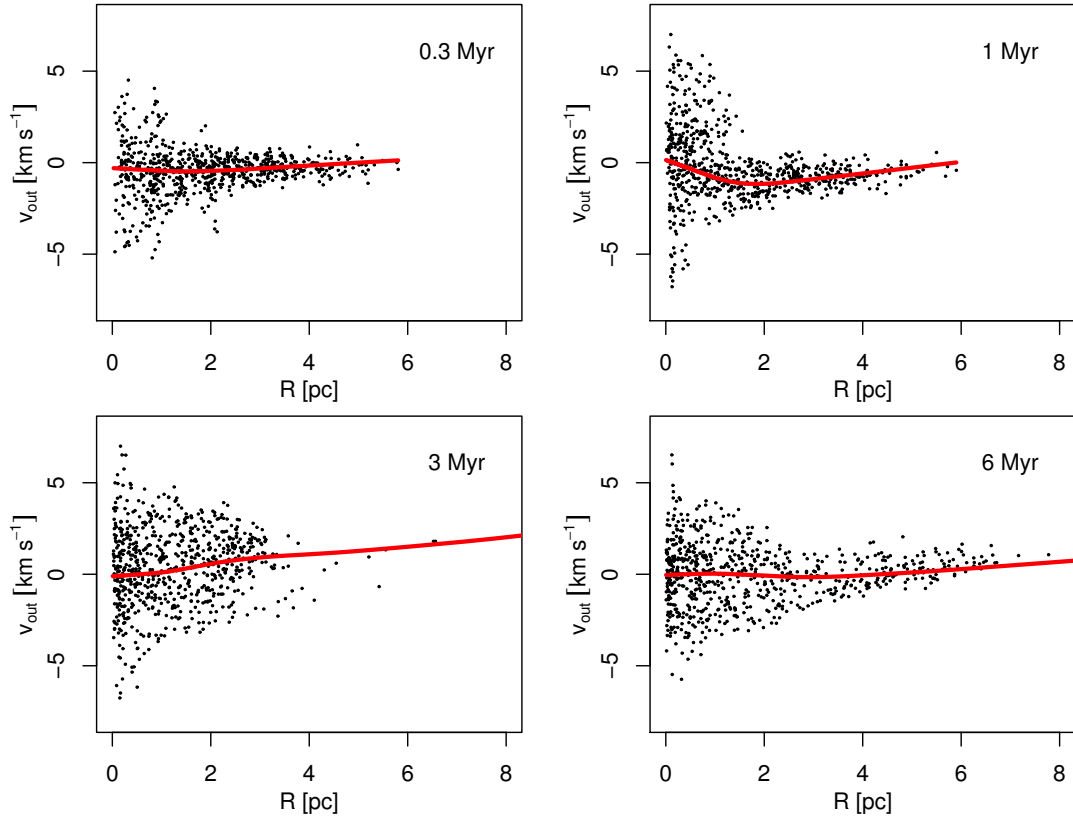


Figure 20. Snapshots of outward velocity v_{out} as a function of distance R from the cluster center in the Sills et al. (2018) simulation at 0.3 Myr, 1.0 Myr, 3.0 Myr, and 6.0 Myr. Only stars with $M > 1 M_{\odot}$ are shown for ease of plotting.

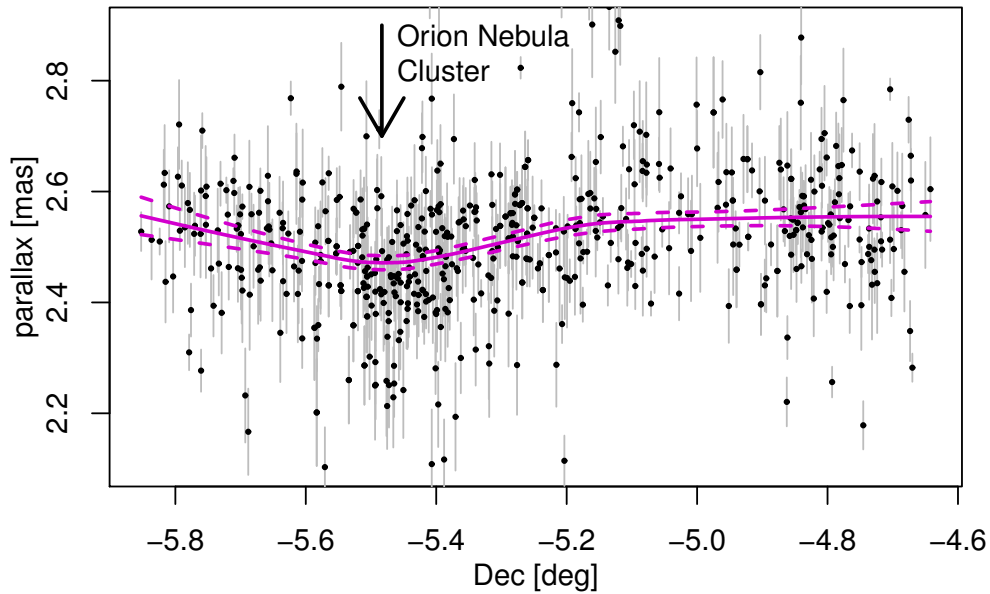


Figure 21. Parallax measurements for probable cluster members in the Orion A clouds, including the ONC. Only points with parallax uncertainties < 0.1 mas are included. The magenta lines show a non-parametric regression line and 95% confidence interval found using the loess regression in the R programming language with options `span = 0.6`, `degree = 1`, `family = "symmetric"`, `iterations = 4`, and `surface = "direct"`.